

# Magnetocaloric-Effect-Enhanced Near-Field Magneto-optical Thermal Switch

Simo Pajovic<sup>1</sup> and Svetlana V. Boriskina<sup>1\*</sup>

*Department of Mechanical Engineering, Massachusetts Institute of Technology, Cambridge, Massachusetts, 02139, USA*

 (Received 30 December 2022; revised 8 June 2023; accepted 16 June 2023; published 24 July 2023)

The magnetocaloric effect is the change in temperature of a magnetic material in response to a change in its magnetization, mediated by an external magnetic field. Since the early 20th century, its main application has been magnetic refrigeration, which has the potential to outperform conventional liquid-vapor refrigerators. In this paper, we combine the magnetocaloric effect with magneto-optical control of near-field radiative heat transfer to introduce an alternative thermal switch with two tuning knobs: a magnetocaloric one that can adjust the temperature gradient and a magneto-optical one that can adjust the conductance of the gap between two materials participating in radiative heat transfer. We consider two representative material systems at room temperature: a Gd-SiC system with magnetocaloric tunability and a Gd-InAs system with both magnetocaloric and magneto-optical tunability. Our model predicts several different operating modes of the thermal switch enabled by the magnetocaloric effect, including one where the flow of heat is reversed. Simultaneously, the magneto-optical response of InAs enables fine-tuning of the spectral heat flux via control of the electromagnetic surface modes. Our work recontextualizes near-field radiative heat transfer between magnetic materials and serves as an example of combining an *i*-caloric effect (the thermal response of a material due to a change in an applied field *i*, where *i* = magneto-, elasto-, electro-, etc.) with a complementary mode of heat transfer to enable new thermal technologies.

DOI: [10.1103/PhysRevApplied.20.014053](https://doi.org/10.1103/PhysRevApplied.20.014053)

## I. INTRODUCTION

The magnetocaloric effect is the phenomenon in which the temperature of a magnetic material changes in response to a change in its magnetization, mediated by an external magnetic field [1]. This can be explained via the change in the magnetic spin entropy, understood in terms of the alignments of the spins relative to the magnetic field. If the spins are randomly aligned initially [Fig. 1(a)], the magnetic field will cause them to align, resulting in a decrease of the spin entropy [Fig. 1(b)]. However, the second law of thermodynamics states that the total entropy of the material must increase or stay the same. In that case, if the material is isolated from its surroundings (i.e., under adiabatic conditions), the lattice entropy increases to guarantee that the second law is satisfied. As a result, the temperature of the material increases [Fig. 1(c)]. Conversely, if the spins are initially aligned parallel to the magnetic field and the magnetic field is removed, collisions between the spins and phonons in the lattice will randomize the spins, increasing the spin entropy and causing a decrease in the lattice entropy. As a result of this, the temperature of the magnetic material decreases.

The magnetocaloric effect was first discovered in 1917 by Weiss and Piccard [2] (according to Ref. [3], this

discovery has commonly been misattributed to Warburg, who discovered a similar but different phenomenon in 1881 [4]). It has been actively studied since 1933 for applications in solid-state refrigeration [5], offering theoretically higher efficiencies than liquid-vapor refrigeration: 30%–60% of the Carnot efficiency (and coefficient of performance, COP, of up to 15) for magnetic refrigerators [6–8], compared to 5%–10% for liquid-vapor refrigerators [7]. It has been argued that magnetic refrigeration can, in theory, approach the Carnot efficiency [9,10]. In addition, magnetic refrigerators can serve as passive regenerators in externally regenerated or nonregenerative refrigeration cycles, which can expand the temperature range of the cycle and achieve temperatures below 1 K [5,11,12]. Beyond the scope of thermal science, it has been proposed that the magnetocaloric effect could be useful for hyperthermia therapy to treat cancer [13–17] and strokes [18] and for the controlled release of drugs [15,16,19,20].

One application of the magnetocaloric effect that has not been fully explored is thermal switching. Because the magnetocaloric effect enables contactless temperature control, it represents a unique opportunity to change temperature gradients in systems that exchange heat and in doing so control the heat transfer between objects, potentially without incurring parasitic losses. In some scenarios in the literature [21], thermal switching is *not* strictly analogous to electrical switching because there are no “true” *on* and *off* states (1 and 0). Instead, the heat transfer—

\*sborisk@mit.edu

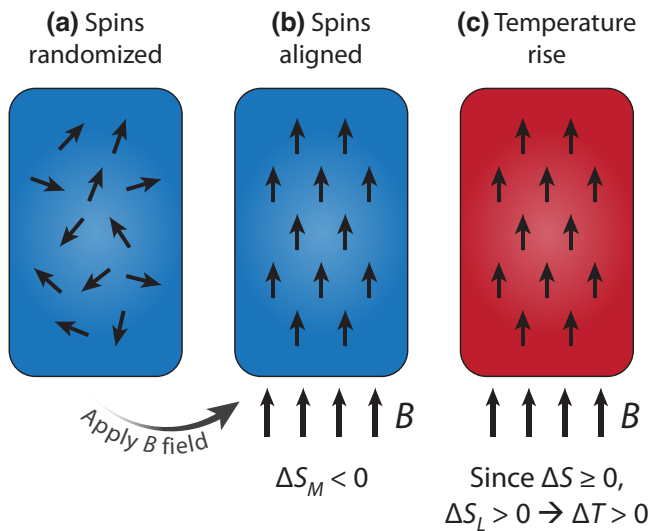


FIG. 1. The magnetocaloric effect. (a) Initially, the magnetic spins are randomly aligned. The total entropy of the magnetic material is  $S = S_M + S_L + S_e$ , where  $S_M$ ,  $S_L$ , and  $S_e$  are the spin, lattice, and electronic entropies, respectively. (b) Under an external magnetic field  $B$ , the spins become aligned, decreasing  $S_M$ . (c) The second law of thermodynamics states that  $\Delta S \geq 0$ , so to guarantee that this is the case,  $S_L$  increases, resulting in a temperature rise  $\Delta T$ .

to current—is modulated through external stimuli, while the temperature gradient—analogue to voltage—is fixed. That is to say, the *conductance* or heat transfer coefficient is modulated, so in reality, these systems are more analogous to potentiometers than electrical switches. On the other hand, systems that modulate the temperature gradient as well as the heat transfer coefficient have the potential to be more analogous to electrical switches. This has been achieved using phase-change materials, whose transport properties can drastically change across the phase-change temperature. For example, theory [22–27] and experiments [28,29] have shown that the metal-insulator transition in  $\text{VO}_2$ , coupled with radiative heat transfer, can be used to implement thermal switches and thermal diodes. In a similar vein, thermal switches based on the magnetocaloric effect can reverse or stop the flow of heat as well as modulate it because of their ability to directly adjust the temperatures of objects in the system and their (magneto-) transport properties without contact. Thus, we believe that “magnetocaloric thermal switches” could be considered more analogous to electrical switches. Through material selection and careful engineering of the magnetic field, it should be possible to design systems with multiple different set points—i.e., crossing points of the magnetic-field-dependent temperatures—that go beyond the scope of thermal switching and into the realm of thermal logic.

At the same time, the idea of using magnetic fields to control heat transfer and achieve thermal switching is not new, especially in the context of thermal radiation. In recent years, there has been great interest in using magnetic fields to control both far-field [30–35] and near-field [36–40] radiative heat transfer via the eigenmodes of Maxwell’s equations. This is possible because magnetic fields break time-reversal symmetry, which lifts the degeneracies of bulk electromagnetic modes and, more importantly, of the surface modes supported at interfaces between materials, which have broken inversion symmetry by nature. In addition to surface plasmon polaritons (SPPs) and surface phonon polaritons (SPhPs), this permits the existence of hyperbolic modes [36,41] and nonreciprocal SPPs, i.e., SPPs whose dispersion relation  $\omega(\mathbf{k})$  is not symmetric  $\omega(\mathbf{k}) \neq \omega(-\mathbf{k})$  [42]. In particular, interfaces supporting nonreciprocal SPPs and systems with broken Lorentz reciprocity in general have garnered interest because of their remarkable ability to direct the flow of heat. For example, it has been shown that Kirchhoff’s law of radiation (the equality of spectral directional emissivity and absorptivity) is broken in nonreciprocal systems [30–32,43], and unidirectional SPPs have been experimentally demonstrated [44]. In the near field, where surface modes (as well as evanescent modes such as frustrated totally internally reflected waves) usually dominate the heat transfer, it has been shown that magnetic fields can offer a high degree of control [36,37] and enable thermal switching [45–47]. The realization of these systems is becoming more practical thanks to the rise of materials that have strong magneto-optical responses in the infrared. Examples include narrow-band-gap semiconductors such as InAs [32,33,35] and InSb [36,37], as well as time-reversal-symmetry-breaking Weyl semimetals such as  $\text{Co}_3\text{Sn}_2\text{S}_2$  [48],  $\text{Co}_2\text{MnAl}$  [49], and  $\text{Co}_2\text{MnGa}$  [50], which are predicted to break Lorentz reciprocity and outperform established magneto-optical materials *without the need for an external magnetic field* [43,51–58].

In this work, we propose combining the magnetocaloric effect and magnetic field control of near-field radiative heat transfer to design a *magnetocaloric-effect-enhanced near-field magneto-optical thermal switch*. We show via rigorous numerical modeling that our system can tune and even reverse the heat transfer via (1) temperature control using the magnetocaloric response and (2) optical mode control using the magneto-optical response. We use a simple model to illustrate a near-field enhanced magnetocaloric thermal switch at room temperature, consisting of two semi-infinite slabs of Gd (a room-temperature magnetocaloric material) and either SiC (a polaritonic material) or InAs (a magneto-optical material that can support surface modes). We theoretically predict the existence of several different modes of operation, which allow us to construct a phase diagram for the thermal switch, and show that the system has a number of knobs that can be turned

to alter its performance for different applications. In Sec. II, we briefly explain our model; molecular field theory is used to calculate the magnetocaloric effect and fluctuational electrodynamics is used to calculate the near-field radiative heat transfer, along with appropriate material models, to be explained in the same section. In Sec. III, we show the results of our calculations and discuss the roles of the magnetocaloric response in the case of the Gd-SiC thermal switch and magneto-optical response in the case of the Gd-InAs thermal switch. This work recontextualizes the role of magnetic materials in systems that exchange heat via thermal radiation (especially in the near field). It points toward an entirely different class of thermal switches that synergize the thermodynamics and optics of magnetism. More broadly, it highlights the potential of *i*-caloric effects [59–61]—defined as the thermal response of a material to a change in an applied field *i* (*i* = magneto-, elasto-, electro-, etc.) and parameterized by either an adiabatic temperature change or an isothermal entropy change—in combination with complementary modes of heat transfer to conceptualize novel solid-state devices.

## II. MATHEMATICAL MODEL OF THE THERMAL SWITCH

In this section, we briefly explain molecular field theory (in the context of the magnetocaloric effect) and fluctuational electrodynamics, the two theoretical formalisms that make up our model. Additionally, we introduce the dielectric tensors of Gd, SiC, and InAs, which are needed to calculate the heat flux. Detailed discussions of each component of our model can be found in the literature since they are established theories; as such, our explanation will be relatively straightforward and will focus on the models' integration and computation.

The system under consideration is shown in Fig. 2(a). It consists of two semi-infinite slabs separated by a vacuum or air gap of width  $d$ , a dielectric material (grey) at a fixed temperature  $T_D = 300$  K, and a magnetocaloric material (blue) at a free temperature  $T_i$ , with the initial temperature difference  $\Delta T_i \equiv T_D - T_i > 0$ , such that the initial heat flux  $Q_i > 0$  flows from the dielectric material to the magnetocaloric material. Initially, the spins inside the magnetocaloric material are randomly oriented, but when an external magnetic field  $\mathbf{B}$  is turned on, they align themselves parallel to  $\mathbf{B}$ , resulting in a temperature change  $\Delta T(T_i, B) > 0$  caused by the magnetocaloric effect. Figure 2(b) shows the case in which  $T_i + \Delta T(T_i, B) > T_D$  and the final heat flux  $Q_f < 0$ , meaning the flow of heat is reversed and, depending on the relative temperature differences,  $|Q_f| \neq |Q_i|$ . If the system is left alone, it will eventually relax toward thermal equilibrium. Note that if the magnetic field is turned off after reaching thermal equilibrium, the temperature of the magnetocaloric material will drop, as previously mentioned. Figure 2(c) summarizes

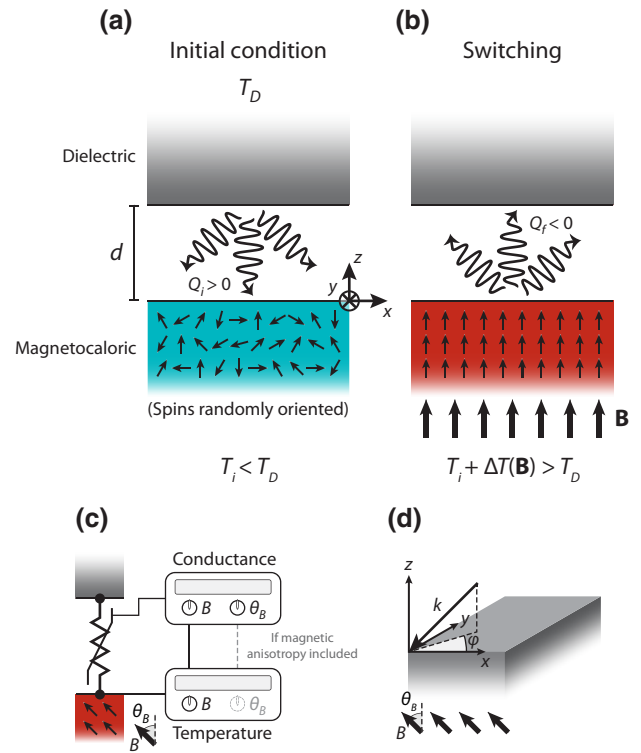


FIG. 2. Principle of operation of the near-field magnetocaloric thermal switch. (a) Initially, two semi-infinite slabs, a magnetocaloric material and a dielectric material at temperatures  $T_i$  and  $T_D$ , are separated by a vacuum or air gap of width  $d$  and participate in radiative heat transfer of heat flux  $Q_i$ . (b) At  $t = 0$ , an external magnetic field  $\mathbf{B}$  is turned on, which changes the magnetization of the magnetocaloric material and causes its temperature to change to  $T_i + \Delta T(\mathbf{B})$ . As a result of the change in temperature and (depending on material selection) magneto-optical response, the heat flux changes to  $Q_f$ . (c) Schematic of the “tuning knobs” of the system. Both the magnitude  $B$  and direction  $\theta_B$  of the external magnetic field can tune the conductance of the gap, while  $B$  can tune the temperature of the magnetocaloric material. Thus,  $B$  couples the tuning knobs. If magnetic anisotropy is included,  $\theta_B$  can play a role as well. (d) Schematic of the coordinate system. The external magnetic field  $\mathbf{B}$  is in the  $x$ - $z$  plane. The azimuthal angle of incidence is  $\varphi$ .

the general idea of the system: the magnitude and direction of  $\mathbf{B}$  serve as tuning knobs for the conductance (via magneto-optical effects) and the temperature at one node (via magnetocaloric effects). In other words, the dielectric material can be thought of as a heat source (or connected to one), and the external magnetic field is used to control both the conductance and temperature of the magnetocaloric material (the receiver) to route the flow of heat into or out of the source as needed.

The picture in Fig. 2 can be generalized in a number of ways, as shown in the Supplemental Material Fig. S1 [62]. (1)  $\Delta T_i$  does not have to be positive. It can be negative, meaning  $Q_i$  flows from the magnetocaloric material to the dielectric, or even zero, meaning  $Q_i = 0$  and the system is

in thermal equilibrium. (2)  $\mathbf{B}$  can point in any direction. Since the heat flux is integrated over all possible directions (to be explained in Sec. II B), only the polar angle  $\theta_B$  matters. (3) The initial magnetic field does not have to be zero. In general, the system can have nonzero initial and final magnetic fields  $\mathbf{B}_i$  and  $\mathbf{B}_f$ , respectively, and the temperature change  $\Delta T$  will be a function of both  $B_i$  and  $B_f$ . In that case, the spins may be more or less aligned depending on  $B_i$  and  $B_f$ ; Fig. S1 in the Supplemental Material [62] illustrates a case in which the spins initially are strongly aligned and become weakly aligned when the magnitude and direction of  $\mathbf{B}$  change.

Lastly, let us comment on material selection. Our choices of Gd, SiC, and InAs can be understood by looking at Fig. 3, which shows how the magnetocaloric and optical responses of these materials overlap with the spectral range of blackbody radiation at room temperature. In the case of the magnetocaloric effect of Gd, the usual  $T$  axis is transformed into wavelength using Wien's law [100] to better illustrate how thermal emitters at or around room temperature can leverage the large  $\Delta T$  values of Gd. (Strictly speaking, it would be more informative to use a "near-field Wien's law" [101], but this can depend on the resonant modes supported by the materials, i.e., plasmonic versus polaritonic.) The bottom two panels show the lossless dispersion relations of SPhPs and SPPs supported by SiC-vacuum and InAs-vacuum interfaces, respectively, calculated using  $k = (\omega/c)\sqrt{\varepsilon(\omega)/[\varepsilon(\omega) + 1]}$ , where  $c$  is the speed of light in vacuum and  $\varepsilon(\omega)$  is the dielectric function of either SiC or InAs [102].

### A. Thermodynamic model of the magnetocaloric effect

To calculate  $\Delta T(T_i, B_i, B_f)$ , we calculate the total entropy  $S$  of the magnetocaloric material as a function of temperature  $T$  at the initial and final values of the magnetic field,  $B_i$  and  $B_f$ , then graphically determine the temperature difference between points  $(T_i, S_i)$  and  $(T_f, S_f)$  on the  $T$ - $S$  diagram under the condition  $S_f = S_i$  (see [103] and Sec. 2 in the Supplemental Material [62]). The total entropy of the magnetocaloric material has three components: the electronic entropy  $S_e$ , the lattice entropy  $S_L$ , and the magnetic spin entropy  $S_M$ ,

$$S = S_e + S_L + S_M. \quad (1)$$

$S_e$  is calculated using tabulated values of the electronic specific heat,  $a_e$  [104],

$$S_e = a_e T. \quad (2)$$

For Gd, the magnetocaloric material of choice in this work,  $a_e = 11 \text{ mJ mol K}^{-2}$  [103,105]. The lattice entropy  $S_L$  is calculated using the Debye model [104],

$$S_L = R \left[ -3 \ln(1 - e^{\theta_D/T}) + 12 \left( \frac{T}{\theta_D} \right)^3 \int_0^{\theta_D/T} \frac{x^3}{e^x - 1} dx \right], \quad (3)$$

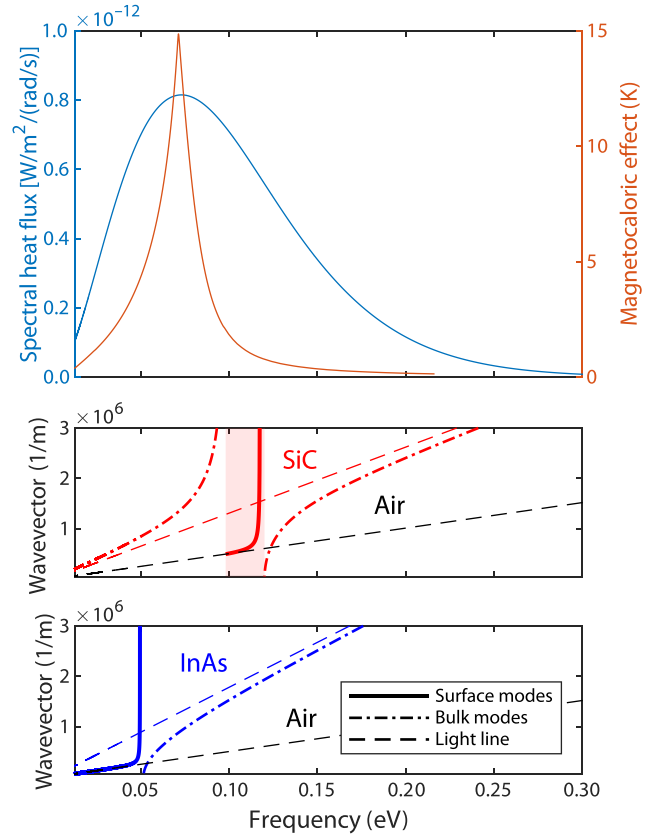


FIG. 3. Material selection. Top: Spectral heat flux of blackbody radiation at room temperature compared to the magnetocaloric effect of Gd in the case of  $B = 0 \rightarrow 7 \text{ T}$ , as a function of frequency. In the case of the magnetocaloric effect, temperature is converted to frequency using Wien's law,  $\omega = 2.431 \times 10^{-4} T [\text{eV}]$ . Middle: The lossless dispersion relation of SPhPs supported by SiC (solid line), along with bulk modes (dash-dotted line) and the light lines in SiC (dashed red line) and air (dashed black line). The shaded area is the reststrahlen band. Bottom: The lossless dispersion relation of SPPs supported by InAs, with the same notation as the middle panel.

where  $R = 8.3145 \text{ mol K}^{-1}$  is the universal gas constant and  $\theta_D$  is the Debye temperature. For Gd,  $\theta_D = 184 \text{ K}$  [103]. Finally, the magnetic spin entropy  $S_M$  is calculated using molecular field theory [1,103], which states that

$$S_M = R \left\{ \ln \left[ \frac{\sinh((2J+1)/2J x)}{\sinh((1/2J)x)} \right] - x B_J(x) \right\}, \quad (4)$$

where  $B_J(x)$  is the Brillouin function,

$$B_J(x) = \frac{2J+1}{2J} \coth \left( \frac{2J+1}{2J} x \right) - \frac{1}{2J} \coth \left( \frac{1}{2J} x \right) \quad (5)$$

and

$$x = \frac{g_J J \mu_B B}{k_B T} + \frac{3\theta_C J B_J(x)}{(J+1)T}. \quad (6)$$

In Eq. (6),  $g_J$  is the Landé  $g$ -factor,  $J$  is the total angular momentum quantum number,  $\mu_B$  is the Bohr magneton,  $\theta_C$  is the Curie temperature, and  $k_B$  is the Boltzmann constant. For Gd,  $g_J = 2$ ,  $J = 7/2$ , and  $\theta_C = 293$  K [103].  $x$  can be thought of as the ratio of the Zeeman energy to  $k_B T$  and is calculated by self-consistently solving Eqs. (5) and (6), which can be done using Newton's method to solve the transcendental equation Eq. (6) or a Taylor series expansion of the Brillouin function to simplify Eq. (6), for example.

Strictly speaking, Eqs. (4)–(6) apply to ferromagnets, but the magnetocaloric effect of antiferromagnets can be calculated by substituting the Néel temperature for  $\theta_C$  [1, 103]. Typically, the magnetocaloric response of a ferromagnetic material is strongest near  $\theta_C$  because it transitions from a ferromagnetic phase (more ordered) to a paramagnetic phase (more disordered), meaning the change in the spin entropy is the largest. The same is true of antiferromagnetic materials near their Néel temperatures, such as Tb [103]. This information is useful for the design of thermal switches based on the magnetocaloric effect because it constrains  $\theta_C$  to be as close as possible to the operating temperature of the system in which the thermal switch will be used.

## B. Fluctuational electrodynamics model of radiative heat transfer

To calculate the heat flux, we use fluctuational electrodynamics, which assumes that thermal radiation originates from random, thermally fluctuating current sources inside each body incorporated into Maxwell's equations [38, 106, 107]. For the system shown in Figs. 2(a) and 2(b) (essentially two semi-infinite, anisotropic, and homogeneous slabs) with the coordinate system shown in Fig. 2(d), the heat flux is

$$Q = \int_0^\infty \frac{d\omega}{2\pi} [\Theta(\omega, T_D) - \Theta(\omega, T_{MC})] \int \frac{d^2\mathbf{q}}{(2\pi)^2} \tau(\omega, \mathbf{q}, d), \quad (7)$$

where  $\mathbf{q}$  is the in-plane wave vector,  $\Theta(\omega, T) = \hbar\omega / (e^{\hbar\omega/k_B T} - 1)$  is the mean energy of a Planck oscillator,  $\tau(\omega, \mathbf{q}, d)$  is the energy transmission coefficient. Additionally,  $\hbar$  is the reduced Planck's constant and  $T_{MC}$  is the temperature of the magnetocaloric material. All the physics of near-field radiative heat transfer is embedded in  $\tau(\omega, \mathbf{q}, d)$ , which is given by

$$\tau(\omega, \mathbf{q}, d) = \begin{cases} \text{Tr}[(I - R_2^\dagger R_2) D_{12} [I - R_1 R_1^\dagger] D_{12}^\dagger], & |\mathbf{q}| < \omega/c, \\ \text{Tr}[(R_2^\dagger - R_2) D_{12} [R_1 - R_1^\dagger] D_{12}^\dagger] e^{-2|k_{0,z}|d}, & |\mathbf{q}| > \omega/c, \end{cases} \quad (8)$$

where  $R_i = \begin{bmatrix} r_i^{pp} & r_i^{ps} \\ r_i^{sp} & r_i^{ss} \end{bmatrix}$ ,  $i = 1, 2$  are the reflection matrices of the planar interfaces,  $D_{12} = (I - R_1 R_2 e^{-2ik_{0,z}d})^{-1}$  is the multiple reflection (or Fabry-Pérot) term, and  $k_{0,z}$  is the out-of-plane ( $z$ ) component of the wave vector in the gap. Additionally,  $I$  is the identity matrix and  $^\dagger$  denotes the conjugate transpose. In  $R_i$ ,  $r_i^{mn}$  denotes the reflection coefficient associated with an outbound  $n$ -polarized wave created by an inbound  $m$ -polarized wave, where  $m, n = s, p$ . In Eq. (8), the first row represents the contribution from propagating waves ( $|\mathbf{q}| < \omega/c$  and  $k_{0,z} \in \mathbb{R}$ ) and the second from evanescent waves ( $|\mathbf{q}| > \omega/c$  and  $k_{0,z} \in \mathbb{I}$ ). Equation (7) is an integral over  $k_x$  and  $k_y$ , where  $\mathbf{q} = k_x \hat{\mathbf{x}} + k_y \hat{\mathbf{y}}$ , but it can be recast as an integral over  $q = |\mathbf{q}|$  and  $\varphi = \arctan(k_y/k_x)$  [see Fig. 2(d)] [58],

$$Q = \int_0^\infty \frac{d\omega}{2\pi} [\Theta(\omega, T_D) - \Theta(\omega, T_{MC})] \int_0^\infty \frac{dq}{2\pi} q \int_0^{2\pi} \frac{d\varphi}{2\pi} \tau(\omega, q, \varphi, d). \quad (9)$$

This facilitates the calculation of the reflection coefficients, which is described in Ref. [58] and Sec. 3 in the Supplemental Material in greater detail [62].

Finally, to calculate the reflection coefficients, we need appropriate models of the dielectric tensors of Gd, SiC, and InAs. This is because the magnetic field affects the motion of free carriers inside Gd and InAs and makes their dielectric responses anisotropic, leading to magneto-optical effects; the dielectric response of SiC is isotropic because it is dominated by phonons, not free carriers. For SiC, we use a fairly standard model of the dielectric function of polaritonic materials [108–110],

$$\varepsilon_{\text{SiC}}(\omega) = \varepsilon_\infty \frac{\omega^2 - \omega_{\text{LO}}^2 + i\Gamma\omega}{\omega^2 - \omega_{\text{TO}}^2 + i\Gamma\omega}, \quad (10)$$

where  $\varepsilon_\infty = 6.7$  is the high-frequency dielectric constant,  $\omega_{\text{LO}} = 0.120$  eV and  $\omega_{\text{TO}} = 0.098$  eV are the longitudinal and transverse optical phonon frequencies, respectively, and  $\Gamma = 0.588$  meV is the damping constant [109]. The dielectric tensor of SiC is diagonal:  $\bar{\varepsilon}_{\text{SiC}}(\omega) = \varepsilon_{\text{SiC}}(\omega)I$ .

For Gd and InAs, we use the so-called gyrotropic Drude-Lorentz model, which is derived using the same equation

$$\bar{\bar{\epsilon}}_{\text{GDL}}(\omega) = \begin{bmatrix} \epsilon_{\infty} - \frac{\omega_p^2(\omega+i\gamma)}{\omega[(\omega+i\gamma)^2-\omega_c^2]} & \frac{i\omega_p^2\omega_c}{\omega[(\omega+i\gamma)^2-\omega_c^2]} & 0 \\ -\frac{i\omega_p^2\omega_c}{\omega[(\omega+i\gamma)^2-\omega_c^2]} & \epsilon_{\infty} - \frac{\omega_p^2(\omega+i\gamma)}{\omega[(\omega+i\gamma)^2-\omega_c^2]} & 0 \\ 0 & 0 & \epsilon_{\infty} - \frac{\omega_p^2}{\omega(\omega+i\gamma)} \end{bmatrix}, \quad (11)$$

where  $\omega_p$  is the plasma frequency,  $\gamma$  is the damping constant, and  $\omega_c = eB/m^*$  is the cyclotron frequency. Usually,  $\omega_p$  is given by  $\omega_p = \sqrt{ne^2/m^*\epsilon_0}$ , where  $n$  is the free carrier density,  $e$  is the elementary charge, and  $\epsilon_0$  is the permittivity of free space. For InAs,  $\epsilon_{\infty} = 12.4$ ,  $\omega_p = 0.181$  eV,  $\gamma = 0.102$  meV,  $n = 7.8 \times 10^{23}$  m<sup>3</sup>, and  $m^* = 0.033m_e$ , where  $m_e$  is the electron mass [32,112]. For Gd, these parameters are not as readily available as for InAs, so we have to make some assumptions. According to experimental data found in the literature, for Gd,  $\epsilon_{\infty} = 1$ ,  $\omega_p = 3.48$  eV, and  $\gamma = 224$  meV [113]. To calculate  $\omega_c$ , we need to know  $m^*$ , which forces us to make an assumption either about  $m^*$  itself or about  $n$ , which allows us to calculate  $m^*$  by way of  $\omega_p$ . We use the free electron model and assume that  $n \approx (2m_e E_F)^{3/2}/3\pi^2 \hbar^3$ , where  $E_F = 0.25$  Ry  $\approx 3.4$  eV [114]. Under this assumption,  $n \approx 2.85 \times 10^{28}$  m<sup>-3</sup>, which is similar to a value reported in the literature [115], and  $m^* \approx 3.24m_e$ .

Finally, Eq. (11) corresponds to the case in which  $\theta_B = 0^\circ$  ( $\mathbf{B}$  pointing in the  $z$  direction). If  $\theta_B \neq 0^\circ$ , the dielectric tensor can be rotated using the transformation  $\bar{\bar{\epsilon}}' = R\bar{\bar{\epsilon}}R^{-1}$ , where

$$R = \begin{bmatrix} 1 & 0 & 0 \\ 0 & \cos \theta_B & -\sin \theta_B \\ 0 & \sin \theta_B & \cos \theta_B \end{bmatrix}. \quad (12)$$

With that, we have all the information we need to perform a parametric study of the thermal switch. A table summarizing the material property data used in this work can be found in Sec. 4 in the Supplemental Material [62].

Before moving on, we remark on the time scales involved in the system under consideration. Although we are not attempting to model the time dependence of temperature and heat flux, we assume that the time scale associated with the magnetocaloric effect is much shorter than the thermal relaxation time associated with cooling or heating the magnetocaloric material via near-field radiative heat transfer (in other words, we assume adiabatic magnetization or demagnetization). According to Kamarád *et al.* [116], the time taken for the temperature of a piece of Gd to change upon magnetization is comparable to the spin relaxation time, on the order of  $10^{-6}$  s. On the other hand,

of motion as the Drude-Lorentz model with the addition of the Lorentz force [32,111],

using the lumped-capacitance model [117], we can estimate the thermal relaxation time associated with cooling or heating the magnetocaloric material via near-field radiative heat transfer:  $\tau \sim mc/hA$ , where  $h$  is the near-field radiative heat transfer coefficient and  $A$  is the surface area of the magnetocaloric material. If we define a characteristic length or thickness  $L = V/A$ , where  $V$  is the volume of the magnetocaloric material, the thermal relaxation time per unit thickness is  $\tau/L \sim \rho c/h$ . Taking  $\rho = 7900$  kg m<sup>-3</sup>,  $c \sim 300$  J kg<sup>-1</sup> K<sup>-1</sup>, and  $h \sim 100$  W m<sup>-2</sup> K<sup>-1</sup> (under the conditions of room temperature and gap width of 100 nm, see [37] and Fig. S10 in the Supplemental Material [62]), we estimate  $\tau/L \sim 4$  min cm<sup>-1</sup>. This is a liberal estimate, but the key takeaway is that the thermal relaxation time is likely to be much longer than the magnetization relaxation time. Our assumption seems to be in good agreement with several experiments [116,118–122], where  $T(t)$  and  $B(t)$  ( $t$  being time) either overlapped or followed each other closely, suggesting that  $T$  changes almost instantly in response to  $B$ , at least relative to the time scale over which  $B$  changes (on the order of 0.1–1 s, depending on whether the field is pulsed or swept).

### III. THERMAL SWITCHING IN GADOLINIUM-BASED SYSTEMS

#### A. Thermal switch with magnetocaloric tunability (Gd-SiC system)

We begin our discussion with the Gd-SiC system mentioned in the introduction. With reference to Fig. 2, Gd is the magnetocaloric material and SiC is the dielectric material. Again, Gd-based systems are of interest because  $\theta_C$  is close to room temperature and, consequently, the magnetocaloric response of Gd is strongest at room temperature. (This is also why Gd is useful for applications in room-temperature magnetic refrigeration and heat pumping [7, 123].)

Before discussing the thermal switching performance, let us go over the thermal radiative properties of the system. As previously mentioned, all the physics of near-field radiative heat transfer is embedded in  $\tau(\omega, \mathbf{q}, d)$ , Eq. (8), so by looking at that, we can understand what to expect in terms of the magneto-optical response. Figure 4 is a plot of  $\tau(\omega, \mathbf{q}, d)$  when  $d = 100$  nm. As it turns out, according

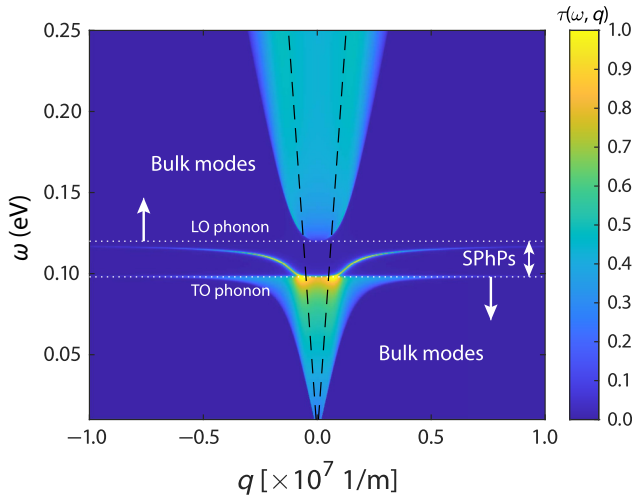


FIG. 4. Transmission coefficient  $\tau(\omega, q)$  between Gd and SiC when  $d = 100$  nm. Because SiC is a polaritonic material (i.e., its dielectric function in the mid- to far-infrared spectral range does not have a free carrier contribution) and the magneto-optical response of Gd is weak in the far infrared, the transmission coefficient is approximately isotropic and independent of the external magnetic field. The dotted white lines denote the phononic band gap between the longitudinal optical (LO) phonon and transverse optical (TO) phonon modes (i.e., the reststrahlen band), where SPhP modes are supported. The dashed black lines denote the light cone,  $\omega = cq$ .

to the model of the dielectric tensor of Gd in Sec. II, the magneto-optical response of Gd is extremely weak in the far infrared, so much so that it can be neglected. As a result of this, the system is essentially isotropic, meaning that  $\tau(\omega, \mathbf{q}, d)$  only depends on  $q$  (and not  $\varphi$  and  $\mathbf{B}$ ). The thermal radiative properties boil down to those of SiC, which are well understood [124–127]—the near-field radiative heat transfer is dominated by bulk (phonon polariton) modes and SPhPs, whose dispersion relations are outside the light line, as can be seen in Fig. 4. Therefore, we can expect the system to have strong magnetocaloric tunability but weak (in fact, negligible) magneto-optical tunability.

To understand the thermal switching performance of the system, we define the switching ratio  $G = Q_f/Q_i$ , where  $Q_i$  is the initial heat flux evaluated using  $\Delta T_i = T_i - T_D$  (recall that  $T_D = 300$  K) and  $Q_f$  is the final heat flux evaluated using  $\Delta T_f = \Delta T_i + \Delta T(B_i, B_f)$ . In Figs. 5(a)–5(c),  $G$  is plotted as a function of  $\Delta T_i$  and  $B_f$ , with each panel corresponding to a different  $B_i$ . Plotting  $G$  in this way reveals the critical points of the system, depicted as the black lines. First, along the dashed lines, where  $\Delta T(B_i, B_f) = -\Delta T_i$ ,  $G = 0$  since  $Q_f = 0$ . In other words, the change in temperature resulting from the magnetocaloric effect equals the initial temperature difference between Gd and SiC, meaning this is a pure *on-off* switching state. The *on-off* switching line separates the regions where  $G > 0$

and  $G < 0$ , i.e., the heat flux is reversed when this line is crossed. Second, along the solid lines, where  $\Delta T_i = 0$ ,  $G = \pm\infty$  (depending on whether you are approaching from the right or left) since  $Q_i = 0$ . In contrast to the previous critical point, this represents a pure *off-on* switching state, since Gd and SiC are in thermal equilibrium to begin with. Third and last, along the dotted lines, where  $B_f = B_i$ ,  $G = 1$  since  $Q_f = Q_i$ . This state seems trivial because the initial and final states are identical, but we consider this a critical line because it separates the regions where  $G > 1$ —heat flux enhancement—and  $0 < G < 1$ —heat flux suppression.

We synthesize these observations about the thermal switching performance of the system to plot a generalized phase diagram, shown in Fig. 5(d). This illustrates the different operating modes of the system, given a value of  $\Delta T_i$ . For example, an application that requires the heat flux to be suppressed or turned off should operate in the lighter red regions or as close to the dashed line as possible. Similarly, an application that requires the heat flux to be enhanced should operate in the darker red regions, and one that requires it to be reversed should operate in the blue regions. Thus, via temperature control, the magnetocaloric effect enables us a wider range of operating modes than conventional thermal switches that utilize near-field radiative heat transfer [45–47, 128–130]. These operating modes can be considered analogous to potentiometers and electrical switches, since there are pure *on* and *off* states.

## B. Thermal switch with magnetocaloric and magneto-optical tunability (Gd-InAs system)

In this section, we discuss a Gd-InAs system, in which we can utilize strategies for thermal switching that are unique to near-field radiative heat transfer. Whereas SiC is a polaritonic material, InAs is a narrow-band-gap semiconductor with a relatively small electronic effective mass, so it is expected to have a strong magneto-optical response in the infrared. As before, we can understand this by looking at  $\tau(\omega, \mathbf{q}, d)$ , which is shown as a function of  $B$  and  $\theta_B$  in Fig. 6. In Fig. 6(a), there is no external magnetic field ( $B = 0$  T), and so the near-field radiative heat transfer is dominated by SPPs, which are isotropic. When the external magnetic field is turned on ( $B = 7$  T) and points out of the plane of the slabs ( $\theta_B = 0^\circ$ ), the transmission coefficient possesses contributions from two kinds of high-momentum evanescent modes at different frequencies, as shown in Fig. 6(b). The mid-frequency (around 0.25–0.52 eV) branches correspond to the SPPs, while the high- (around 0.52–0.57 eV) and low-frequency (less than around 0.25 eV) branches correspond to hyperbolic modes—a special kind of frustrated totally internally reflected mode with evanescent fields in the vacuum gap. The hyperbolic modes are permitted to exist because the

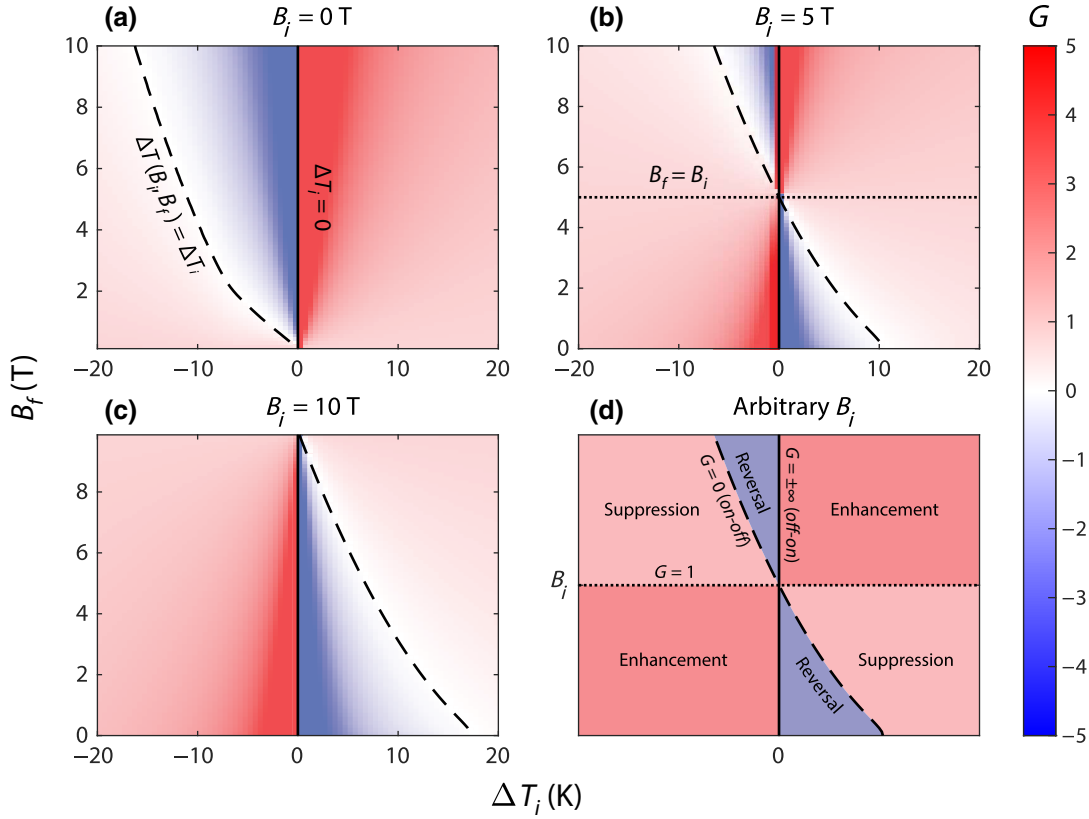


FIG. 5. Switching ratio  $G = Q_f/Q_i$  between Gd and SiC as a function of  $\Delta T_i$  and  $B_f$  for initial magnetic fields  $B_i$  of (a) 0 T, (b) 5 T, and (c) 10 T. The temperature of SiC is fixed,  $T_D = 300$  K. (d) Generalized phase diagram for the Gd-SiC thermal switch. The dashed black line shows the critical point where  $\Delta T(B_i, B_f) = -\Delta T_i$ , or  $G = 0$  since  $Q_f = 0$ . The solid black line shows the critical point where  $\Delta T_i = 0$ , or  $G = \pm\infty$  since  $Q_i = 0$ . The dotted black line shows the critical point where  $B_f = B_i$ , or  $G = 1$  since  $Q_f = Q_i$ .

magnetic field modifies both the on- and off-diagonal components of the dielectric tensor of the magneto-optical material [see Eq. (11)], introducing anisotropy similar to a uniaxial crystal with its optical axis perpendicular to its surface. The material can support hyperbolic modes if the in-plane diagonal components of the dielectric tensor ( $\epsilon_{xx} = \epsilon_{yy}$ ) have the opposite sign to the out-of-plane component ( $\epsilon_{zz}$ ) because of the action of the magnetic field [36]. In other words, the hyperbolic modes exist in the bands where the condition  $\text{Re}[\epsilon_{xx}]\text{Re}[\epsilon_{zz}] < 0$  is satisfied [shown in Fig. 6(b) and Supplemental Material Fig. S7 [62]], and they contribute to the near-field heat radiative transfer along with the SPPs. For this out-of-plane orientation of the external magnetic field, the propagation of both SPPs and the hyperbolic modes remains isotropic and reciprocal in-plane (i.e., with respect to  $\varphi$ ) [36,131]. Because the spectral characteristics of the modes supported by the system have changed, the spectral and total heat fluxes change as well. Thus, this change in the spectral heat flux, shown in Supplemental Material Fig. S10 [62], serves as an additional tuning mechanism to control the magnitude of the heat flux, especially by opening additional channels for radiative heat transfer in the system.

The system can be tuned further by changing the direction of  $\mathbf{B}$ . When  $\theta_B \neq 0^\circ$ , the in-plane propagation of SPPs and hyperbolic modes becomes nonreciprocal (i.e., direction dependent and asymmetrical) owing to the broken time-reversal and now inversion symmetries of the system. This manifests via the shifting of the SPP branches corresponding to forward- and backward-propagating modes along the same axis to different frequencies and changes in their losses. Furthermore, because one of the SPP branches (the  $q > 0$  one) blueshifts, it creates an anticrossing point with the hyperbolic modes that are at a higher frequency [see Figs. 6(b) and 6(c) and Supplemental Material Fig. S11 [62]]. These changes affect the maximum value of  $q$  contributing to the heat flux carried by each mode. The directionality of the nonreciprocal SPPs is maximized when  $\theta_B = 90^\circ$  ( $\mathbf{B}$  parallel to the plane of the slabs). This is shown in Fig. 6(c). In this case, not only is time-reversal symmetry broken by  $\mathbf{B}$ , but inversion symmetry is also broken because  $\mathbf{B}$  lies in the plane of the slabs and the materials on the opposite sides of the gap are dissimilar. Indeed, it has been recognized that in order to observe nonreciprocity, both time-reversal symmetry and inversion symmetry must be broken [132–135]. Thus, based on Fig.

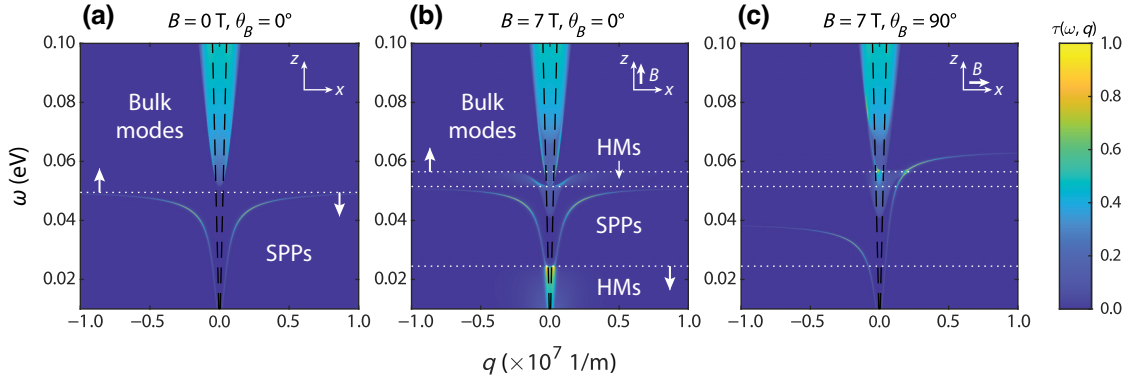


FIG. 6. Transmission coefficient  $\tau(\omega, q)$  between Gd and InAs when  $d = 100$  nm, showing the dependence on the magnitude and direction (i.e., polar angle) of the magnetic field,  $B$  and  $\theta_B$ . (a)  $B = 0$ . The heat flux is dominated by SPPs supported by InAs. (b)  $B = 7$  T and  $\theta_B = 0^\circ$  (magnetic field pointing out of the surface). The magnetic field breaks time-reversal symmetry and introduces anisotropy by changing the diagonal components of the dielectric tensor and introducing the off-diagonal ones. This creates two spectral ranges where hyperbolic modes exist and contribute to the radiative heat transfer, in addition to SPPs. (c)  $B = 7$  T and  $\theta_B = 90^\circ$  (magnetic field pointing parallel to the surface). The SPPs and hyperbolic modes split into distinct nonreciprocal branches at different frequencies *and* wave vectors because the magnetic field breaks time-reversal symmetry *and* inversion symmetry. The anticrossing point between the forward-propagating ( $q > 0$ ) SPPs and hyperbolic modes can be observed at around 0.057 eV. The dashed black lines denote the light cone,  $\omega = cq$ . The coordinate system of the plane of incidence ( $\varphi = 0^\circ$ ) and the magnetic field vector, if it exists, are shown at the top right of each plot. SPPs, surface plasmon polaritons; HMs, hyperbolic modes.

6, we can expect the Gd-InAs system to have both magnetocaloric tunability *and* magneto-optical tunability, in contrast to the Gd-SiC system.

Similarly to the Gd-SiC system, we evaluate the thermal switching performance of the Gd-InAs system using the switching ratio, but in this case, we can break it down into multiple processes to understand the relative contributions of the magnetocaloric and magneto-optical responses. We consider a system where the magnitude of the initial magnetic field is  $|\mathbf{B}_i| = B_i = 5$  T, which should have a magnetocaloric response similar to Fig. 5(b). We define process  $1 \rightarrow 2$  as the rotation of  $\mathbf{B}_i$  from  $0^\circ$  to  $\theta_B$ , as shown in Fig. 7(a). Then, the switching ratio associated with process  $1 \rightarrow 2$  is  $G_{1 \rightarrow 2} = Q_2/Q_1$ , where  $Q_1$  and  $Q_2$  are evaluated at  $0^\circ$  and  $\theta_B$ , respectively, all else being equal. Likewise, we define process  $2 \rightarrow 3$  as the change of the magnetic field from  $B_i$  to  $B_f = B_i + \Delta B$ , as shown in Fig. 7(b), with the associated switching ratio being  $G_{2 \rightarrow 3} = Q_3/Q_2$ . The total switching ratio,  $G_{1 \rightarrow 3} = Q_3/Q_1$ , is the product of the broken-down switching ratios:  $G_{1 \rightarrow 3} = G_{1 \rightarrow 2} \times G_{2 \rightarrow 3}$ .

Figure 7(a) shows  $G_{1 \rightarrow 2}$  as a function of  $\theta_B$ . As can be seen, rotating the magnetic field gradually changes the heat flux, as the propagation of SPPs and hyperbolic modes becomes more nonreciprocal and frequency-shifted (as in Fig. 6 and Supplemental Material Fig. S11 [62]). However, the tunability is relatively weak:  $G_{1 \rightarrow 2} \approx 0.92$  at best, compared to factors of close to 10 predicted for near-field thermal switches based on different material systems in the literature [46,58]. The reason is that the *resonant* surface modes supported by Gd and InAs

exist at entirely different frequencies, meaning these surface modes cannot couple to each other. Stronger tunability can be achieved when the materials are identical or support resonant surface modes in overlapping frequency ranges [124,136–138]. Under these conditions, the resonant surface modes on each side can electromagnetically couple, further increasing the near-field radiative heat transfer across the gap. In the Gd-InAs system, the presence of Gd modulates the photon density of states across the gap and permits the SPPs supported by InAs to exist at higher wave vectors (similar to the effect of a prism). The contribution from higher-momentum states increases the heat flux, but not as much as if both materials were identical. As a result, the Gd-InAs system exhibits magneto-optical tunability, but there is room for improvement.

Figure 7(b) shows  $G_{2 \rightarrow 3}$ , which is not sensitive to  $\theta_B$ . Clearly, for this material system, the magnetocaloric tunability can be much stronger than the magneto-optical tunability and has a much wider range of switching ratios. The plots of  $G_{2 \rightarrow 3}$  are similar to those of  $G$  in Fig. 5, which is expected because both systems are Gd-based. In fact, it is worth pointing out that the temperature dependence of the magneto-optical tunability is not that strong over the range of temperatures we are interested in. Thus, the system has one switching mechanism that is relatively sensitive to temperature—the magnetocaloric response—and another that is not—the magneto-optical response. In this way, the two switching mechanisms are somewhat decoupled but synergistic. However, in this case, the magnetocaloric tunability is dominant, as can be seen in Fig. 7(c), which

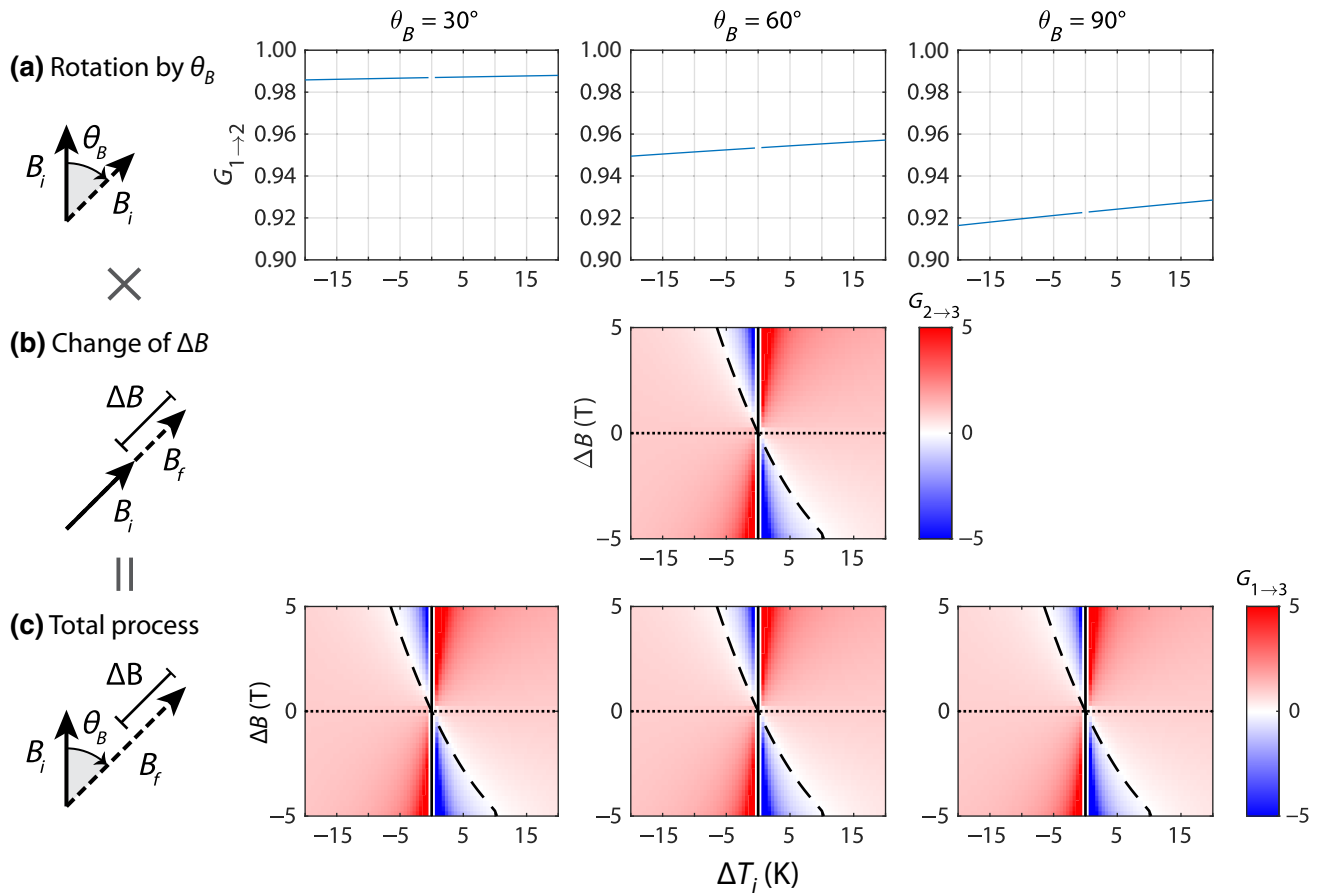


FIG. 7. Switching ratios between Gd and InAs as a function of  $\Delta T_i$ ,  $\Delta B$ , and  $\theta_B$  for initial magnetic field  $B_i = 5$  T. The temperature of InAs is fixed,  $T_D = 300$  K. (a) Switching ratio after the first process, rotation of the magnetic field from  $0^\circ$  to  $\theta_B$ , defined as  $G_{1 \rightarrow 2} = Q_2/Q_1$ . The dependence on  $\theta_B$  is shown across the columns. (b) Switching ratio after the second process, change of the magnetic field from  $B_i$  to  $B_i + \Delta B$ , defined as  $G_{2 \rightarrow 3} = Q_3/Q_2$ . Only one plot is shown because  $G_{2 \rightarrow 3}$  is not sensitive to  $\theta_B$ . (c) Total switching ratio, defined as  $G_{1 \rightarrow 3} = G_{1 \rightarrow 2} \times G_{2 \rightarrow 3} = Q_3/Q_1$ .

depicts  $G_{1 \rightarrow 3}$ . Because the magneto-optical tunability is relatively weak, it does not significantly modulate the magnetocaloric tunability, and so the dependence on  $\theta_B$  is not that strong—although there are ways in which this can be remedied, to be discussed in Sec. IV. Nonetheless, we believe that the Gd-InAs system highlights the potential of near-field magnetocaloric thermal switches.

Our results demonstrate that the advantage of using near-field thermal radiation over conduction as the heat transfer mechanism is twofold. First, except under certain conditions [139,140], the effect of magnetic fields on phonons is much weaker than on electrons, which are typically responsible for magneto-optical effects. This can be understood by comparing the cyclotron frequencies of an electron and an ion: if  $\omega_c = qB/m^*$ , where  $q$  is charge,  $B$  is magnetic field, and  $m^*$  is effective mass, the cyclotron frequency of the ion will be a few orders of magnitude smaller than that of the electron because the mass of *just one* nucleon is 2,000 times larger than that of the electron. If  $B \sim 1$  T, we can estimate that  $\omega_c$  is  $2 \times 10^{-4}$  THz for

the ion and  $2 \times 10^{-1}$  THz for the electron. In fact, if the effective mass of the electron is small (such as in narrow-band-gap semiconductors), its cyclotron frequency is even larger, falling in the far infrared, which is the spectral range of most thermal emitters at room temperature. This offers the ability to achieve strong tunability of the heat transfer.

Second, unlike conduction where the point of contact or interface cannot be controlled *in operando*, in near-field thermal radiation, the gap width  $d$  can be controlled (i.e., mechanically, hypothetically via magnetostriction). The dependence of the heat flux and heat transfer coefficient on  $d$  is well established [141–143]. Generally speaking, as  $d$  decreases, the coupling between the resonant surface modes supported by each material becomes stronger, and the coupled modes supported by the gap can have higher momenta. This increases the heat flux according to Eq. (9) and should strengthen the magneto-optical tunability [36,37,58]. On the other hand, as  $d$  increases, the gap widens and the contribution to the heat flux from coupled modes decreases until the objects are in the far field.

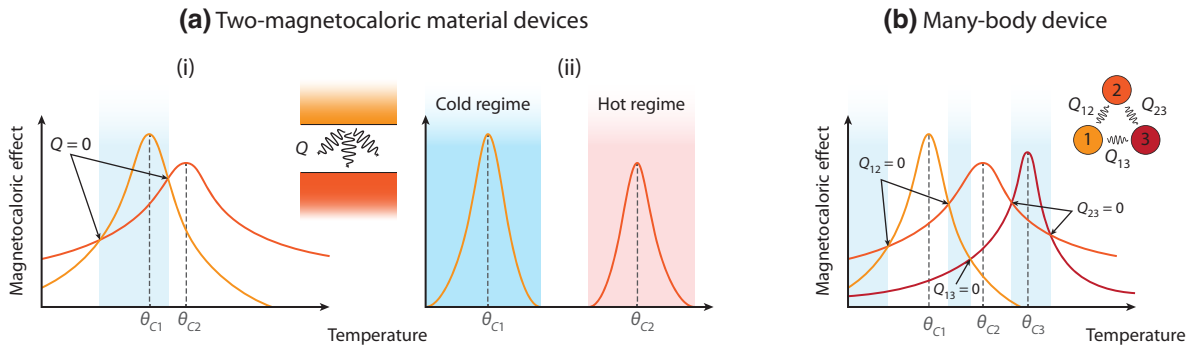


FIG. 8. Outlook for near-field enhanced magnetocaloric thermal switches. (a) Concepts for two-magnetocaloric material devices. (i) If the two magnetocaloric materials are chosen such that their responses overlap, the crossing points should lead to multiple phases and critical points richer than Fig. 5(d). (ii) If instead their responses are far apart, the system should behave similarly to the Gd-SiC system in Fig. 5(d), but with distinct “hot” and “cold” regimes. (b) Many-body devices could have even more complex behavior than two-body devices, including unique many-body magneto-optical effects [39,40,151].

In this regime, the magneto-optical tunability should be the weakest. However, in the case of the Gd-InAs system, the magneto-optical tunability is maximized at distances between the far field ( $d \gtrsim 1 \mu\text{m}$ ) and the extreme near field ( $d \lesssim 10 \text{ nm}$ ). This is shown in Fig. S14 in the Supplemental Material [62]. The reason for this is that the momenta of hyperbolic modes are not as high as those of SPPs: as  $d$  decreases, the contribution to the heat flux from SPPs starts to dominate, while the contribution from hyperbolic modes changes little. This can be seen in Fig. S14(c) in the Supplemental Material [62], which shows  $\tau(\omega, \mathbf{q}, d)$  when  $d = 10 \text{ nm}$ . Although the external magnetic field splits the

SPPs into forward- and backward-propagating branches, this alone does not lead to strong magneto-optical tunability in the Gd-InAs system. Thus, it is favorable to operate at a value of  $d$  at which hyperbolic modes and SPPs have comparable momenta (at least without mode matching, to be discussed in the following section).

Finally, the entropy of radiation is different from that of conduction. Whereas the latter typically equals  $Q/T$ , where  $Q$  is the heat flux and  $T$  is the temperature, the former is proportional to  $Q/T$  and can take on a range of values depending on the frequency of radiation (i.e., energy of emitted photons) [144–148]. This has implications for the COP of devices such as magnetic refrigerators and will be a subject of our future work.

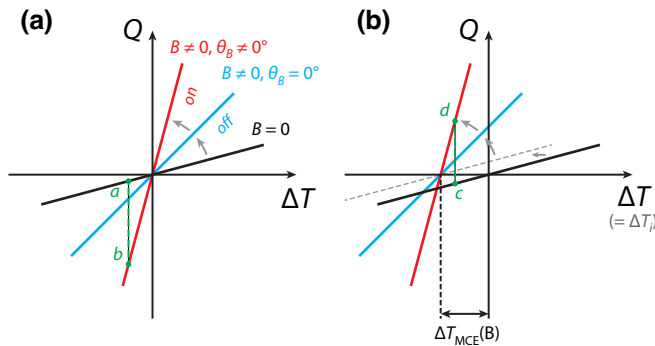


FIG. 9. Difference between a more typical thermal switch [21] and the one presented in this work. (a) As a function of  $B$  and  $\theta_B$ , the slope of the  $Q - \Delta T$  curve changes, and the figure of merit is the ratio of the slopes in the *on* and *off* states. The thermal switch can operate between any two points along line  $a$ - $b$  (the dashed green line), for example. (b) In this work,  $\Delta T$  is a function of  $B$ . As a result, changing  $B$  not only changes the slope of the  $Q - \Delta T$  curve but also shifts it along the  $\Delta T$  axis by an amount equal to the temperature change caused by the magnetocaloric effect  $\Delta T_{MCE}(B)$  (if we interpret  $\Delta T$  in Ref. [21] as being analogous to our definition of  $\Delta T_i$ ). The thermal switch can operate along line  $c$ - $d$ , for example, and the flow of heat can be reversed.

#### IV. CONCLUSION AND OUTLOOK

In this work, we propose an alternative type of thermal switch which leverages both the magnetocaloric effect and magneto-optical control of near-field radiative heat transfer. We predict the performance of two devices based on Gd, which has one of the strongest magnetocaloric responses at room temperature. We show that both systems have a number of different modes of operation where different switching ratios can be achieved, and in fact, the flow of heat can be reversed because the magnetocaloric effect enables direct control of the temperature difference between objects. The devices discussed in this work highlight the potential of solid-state devices that combine *i*-caloric effects [61] with complementary modes of heat transfer. Additionally, this work recontextualizes the role of magnetic materials in systems that exchange heat via thermal radiation, suggesting that previous models may need to be revisited and account for the magnetocaloric effect. Another benefit of the magnetocaloric effect is that it is well suited to a wide range of operating

temperatures—from cryogenic to high-temperature applications, as illustrated in Supplemental Material Fig. S12 [62]—because  $\theta_C$  sets the temperature of the maximum magnetocaloric response.

However, with regard to near-field magnetocaloric thermal switches, there is room for improvement in terms of their predicted thermal switching performance. The weakness of the Gd-InAs system is that the magneto-optical tunability is weak compared with the magnetocaloric tunability. Ideally, the switching ratios associated with each response should be as large as possible. To achieve this, the coupling between the resonant surface modes supported by each material must be as strong as possible. This can be achieved in multiple ways. Obviously, material selection can play a role, but the constraints depend on the operating temperature—because this sets the thermal wavelength, according to Wien’s law [100]—and can be strict. For thermal switch operation at room temperature, for example, the magnetocaloric material must have a  $\theta_C$  close to room temperature and support resonant surface modes in the far infrared. The magneto-optical response does not necessarily have to be strong (so the surface modes dominating the heat transfer can be SPhPs, for example), although it would be better if that were the case. In fact, it should be noted that surface texturing can be used to tailor the spectral properties of the near-field thermal radiation and thereby achieve resonant, large heat transfer at a given frequency or even multiple frequencies [149,150]. Alternatively, a layer of magneto-optical material identical to the one on the other side of the gap can be deposited on the surface of the magnetocaloric material, enhancing the coupling across the gap via mode matching. It would be even better if, instead of a magnetocaloric and a magneto-optical material, the system consisted of two magnetocaloric materials with the aforementioned magneto-optical responses and slightly different  $\theta_C$  that are relatively close to room temperature. If this were the case, their magnetocaloric responses would have one or more crossing points, as shown in Fig. 8(a)(i). This could lead to a wider range of different modes of operation and thermal logic, especially if extended to many bodies [Fig. 8(b)]. Alternatively, it may be desirable to design a system consisting of two magnetocaloric materials with *disparate*  $\theta_C$  so that the system essentially has two operating regimes—one at a low temperature and one at a high temperature, so that there is little overlap between the two. This is shown in Fig. 8(a)(ii).

There are other optimizations that could be made to the system through careful material selection and engineering. Since the resonant frequencies of the surface modes are magnetic field dependent, the magnetocaloric response could be optimized so that the thermal wavelength shifts to maximally populate those levels. In fact, one could make use of the so-called near-field Wien’s law [101] to accurately perform this optimization. Although the magnetic

field dependence of the magnetocaloric effect appears to be monotonic at low magnetic fields [103], the strength of the magneto-optical response is not, at least according to the gyrotropic Drude-Lorentz model, Eq. (11). In Supplemental Material Fig. S8 [62], we plot the antisymmetry figure of merit, defined as the ratio of the matrix norms of the antisymmetric and symmetric parts of the dielectric tensor [53]. This can be considered a metric of how strong we should expect the magneto-optical response to be since it originates from the off-diagonal components of the dielectric tensor. For InAs modeled according to Eq. (11), the antisymmetry figure of merit suggests that the magneto-optical response has an optimum.

An additional and potentially useful refinement one can make is to account for magnetocrystalline anisotropy when calculating the magnetocaloric effect. In this work, we neglect it, but in reality, the magnetocaloric response depends on the direction of the magnetic field relative to the easy and hard axes [1]. This means that rotating the magnetic field will change both the magneto-optical response and induce an additional magnetocaloric response, meaning processes  $1 \rightarrow 2$  and  $2 \rightarrow 3$  in Fig. 7 cannot be decoupled. For a system where two distinct tuning knobs are desirable (“coarse” and “fine”), this could be considered disadvantageous. From the perspective of maximizing the switching ratio, however, this could be an advantage; since the magnetic field tends to blueshift some of the resonant frequencies of the surface modes, as can be seen in Fig. 6, an additional increase in temperature could help to populate those levels more. In the case of Gd, its magnetocrystalline anisotropy is relatively low at cryogenic temperatures [152], but it can strongly vary with temperature near  $\theta_C$  [153].

Moreover, although we model the objects participating in near-field radiative heat transfer as semi-infinite slabs, in order to accurately model the spatial and temporal temperature variations of the objects, their finite sizes and shapes must be considered. There are many ways to calculate the heat flux between finite-sized objects, where the view factors between the objects are not unity, even when many objects are involved. These include scattering formalisms such as those used by Krüger *et al.* [154] and Zhu and Fan [39] and numerical methods such as the boundary-element method [155–158] and volume-integral-equation method [159]. However, depending on the length scale of the objects, there could be other complications, mostly related to accurately modeling the total magnetic field inside and outside the magnetocaloric material. For one, shape anisotropy resulting from the shape of the magnetocaloric material can affect the temperature change caused by the magnetocaloric effect, although this can be lumped together with magnetocrystalline anisotropy. More importantly, since the vast majority of magnetocaloric materials are magnetic materials, they should generate stray fields (i.e., magnetic fields outside the magnet itself). The

magnitude, direction, and spatial distribution of the stray field depend on the size and shape of the magnet, which can be analytically or numerically modeled using magnetostatics (solving Poisson’s equation [152], finite-element analysis, etc.). Crucially, the stray field will affect the total magnetic field acting on the other objects, especially if they are made of magnetic materials as well. In the latter case, the magnetic field distribution inside the objects—regardless of the external (applied) magnetic field—could become quite sophisticated. For example, if the spatial distribution of the magnetic field is not very uniform, the dielectric tensors of the objects will vary spatially, which could require a gradient-index approach.

In Sec. 10 of the Supplemental Material [62], we show how one could account for the stray field generated by Gd using a simplistic refinement to our model. The key takeaway is that the stray field changes both the magnitude and direction of the total magnetic field acting on the magneto-optical material. Essentially, it shifts the switching ratio  $G_{1\rightarrow 2}$  in Fig. 7(a), which is a function of  $B$  and  $\theta_B$ :  $G_{1\rightarrow 2}(B, \theta_B) \rightarrow G_{1\rightarrow 2}(B + \delta B, \theta_B + \delta\theta_B)$ , where  $\delta B$  and  $\delta\theta_B$  are functions of the magnetization of the magnetocaloric material  $M$  and defined in Sec. 10 in the Supplemental Material [62]. The general trends observed in Figs. 6 and 7 should hold. In fact, the stray field could be considered beneficial in the sense that the total magnetic field acting on the magneto-optical material will be larger than the applied magnetic field  $B$ . Practically, this means that a smaller  $B$  is required to achieve a desired magneto-optical response, which can make the thermal switch easier to implement since applying larger magnetic fields can be cumbersome and expensive.

As a final point of discussion, in this work, we use the heat flux switching ratio (sometimes referred to as “contrast” in the literature) as a figure of merit (FOM). A commonly used FOM for thermal switches embedded in a comprehensive switch-environment system model is based on the temperature difference of the cold side in the *on* and *off* states (see, e.g., Ref. [160]) under a fixed hot side temperature. In this scenario, the cold side is thermally coupled to both the environment and—through the variable-conductance switch region—to the temperature-controlled hot side. This FOM definition is not applicable to the model discussed in this work, which only evaluates the switch region performance and where the cold side acts as a fixed-temperature thermal bath. Furthermore, in the systems analyzed in this work, the external stimulus (i.e., magnetic field) not only modifies the conductance across the gap but also directly sets the difference between the *on*- and *off*-state hot side temperatures. The switching effect under this scenario is fundamentally different from the case when the external stimulus and the temperature difference are independently controlled, as illustrated in Fig. 9 [21]. It is also transient in nature and allows one to cyclically pump heat to and from

the environment via a noncontact radiative-heat-transfer mechanism [161].

For practical applications in *i*-caloric solid-state cooling and heating, the FOM characterizing the energy efficiency of the switch could be defined as the ratio of the change in the total heat flux (the amount of power we switch) to the power required to magnetize the magnetocaloric material (the amount of power we have to put in). To properly evaluate this type of FOM, a more detailed model needs to be developed, which accounts for the method used to generate the applied magnetic field (e.g., a permanent magnet, an electromagnet, or a superconducting magnet), the sizes, shapes, and thermal masses of the materials comprising the hot and the cold sides of the switch, as well as the rate of their energy exchange with the environment and, if applicable, the type of the thermodynamic cycle the magnetocaloric pump will be operating in. Prior work has shown that the COP of magnetocaloric solid-state heat pumps operating in the Brayton cycle—which accounts for both the losses in the materials as well as loss associated with the cycle-related irreversibility during the adiabatic application and removal of external stimuli—can significantly exceed the typical COP values of conventional vapor-compression systems [15,60,162]. Furthermore, we believe the advantages of *i*-caloric thermal switches based on radiative rather than conductive or convective heat transfer are (i) the noncontact nature of their operation and (ii) the switch ability to modulate both the temperature and the surface-mode-driven heat-transfer rate, potentially allowing for more flexibility in the system design. A detailed analysis of the thermodynamic properties of heat pumps based on *i*-caloric, radiative thermal switches will be a subject of our future work.

## ACKNOWLEDGMENTS

We thank Miss Adela Li for advice on data visualization and Professor Sean Lubner for helpful discussions on potential applications of thermal switching based on the magnetocaloric effect. We also thank Professor Caroline Ross and Dr. Rohith Mittapally for helpful discussions on stray fields. This work is supported by ARO MURI (Grant No. W911NF-19-1-0279) via U. Michigan. S.P. gratefully acknowledges support from the NSF GRFP under Grant No. 2141064.

- 
- [1] A. M. Tishin and Y. I. Spichkin, *The Magnetocaloric Effect and Its Applications*, 1st ed. (Institute of Physics Publishing, Bristol, UK, 2003).
  - [2] P. Weiss and A. Piccard, Le phénomène magnéto-calorique, *J. Phys. Theor. Appl.* **7**, 103 (1917).
  - [3] A. Smith, Who discovered the magnetocaloric effect?, *Eur. Phys. J. H* **38**, 507 (2013).
  - [4] E. Warburg, Magnetische Untersuchungen, *Ann. Phys.* **249**, 141 (1881).

- [5] W. F. Giauque and D. P. MacDougall, Attainment of Temperatures Below  $1^\circ$  Absolute by Demagnetization of  $\text{Gd}_2(\text{SO}_4)_3 \cdot 8\text{H}_2\text{O}$ , *Phys. Rev.* **43**, 768 (1933).
- [6] C. Zimm, A. Jastrab, A. Sternberg, V. Pecharsky, K. Gschneidner, Jr., M. Osborne, and I. Anderson, Description and performance of a near-room temperature magnetic refrigerator, *Adv. Cryog. Eng.* **43**, 1759 (1998).
- [7] B. F. Yu, Q. Gao, B. Zhang, X. Z. Meng, and Z. Chen, Review on research of room temperature magnetic refrigeration, *Int. J. Refrig.* **26**, 622 (2003).
- [8] L. D. Kirol and M. W. Dacus, in *Advances in Cryogenic Engineering*, edited by R. W. Fast (Springer US, Boston, MA, 1988), Vol. 33, pp. 757–765.
- [9] G. V. Brown, Magnetic heat pumping near room temperature, *J. Appl. Phys.* **47**, 3673 (1976).
- [10] W. A. Steyert, Stirling-cycle rotating magnetic refrigerators and heat engines for use near room temperature, *J. Appl. Phys.* **49**, 1216 (1978).
- [11] S. Jeong, AMR (active magnetic regenerative) refrigeration for low temperature, *Cryogenics (Guildf)* **62**, 193 (2014).
- [12] J. A. Barclay, Active and passive magnetic regenerators in gas/magnetic refrigerators, *J. Alloys Compd.* **207–208**, 355 (1994).
- [13] E. Zatssepina, A. M. Tishin, P. W. Egolf, and D. Vuarnoz, in *Third International Conference on Magnetic Refrigeration at Room Temperature* (Des Moines, ID, ID, 2009).
- [14] Y. Qu, J. Li, J. Ren, J. Leng, C. Lin, and D. Shi, Enhanced magnetic fluid hyperthermia by micellar magnetic nanoclusters composed of  $\text{Mn}_x\text{Zn}_{1-x}\text{Fe}_2\text{O}_4$  nanoparticles for induced tumor cell apoptosis, *ACS Appl. Mater. Interfaces* **6**, 16867 (2014).
- [15] A. M. Tishin and Y. I. Spichkin, Recent progress in magnetocaloric effect: Mechanisms and potential applications, *Int. J. Refrig.* **37**, 223 (2014).
- [16] A. M. Tishin, Y. I. Spichkin, V. I. Zverev, and P. W. Egolf, A review and new perspectives for the magnetocaloric effect: New materials and local heating and cooling inside the human body, *Int. J. Refrig.* **68**, 177 (2016).
- [17] A. Osman, E. Seçilmi, and A. Ekicibil, New application area for magnetocaloric materials: Hyperthermia method, *J. Mol. Struct.* **1231**, 130010 (2021).
- [18] R. Iglesias-Rey, A. Vieites-Prado, B. Argibay, F. Campos, M. Bañobre-López, T. Sobrino, J. Rivas, and J. Castillo, Magnetocaloric effect for inducing hypothermia as new therapeutic strategy for stroke: A physical approach, *J. Appl. Biomed.* **15**, 33 (2017).
- [19] J. Li, Y. Qu, J. Ren, W. Yuan, and D. Shi, Magnetocaloric effect in magnetothermally-responsive nanocarriers for hyperthermia-triggered drug release, *Nanotechnology* **23**, 505706 (2012).
- [20] A. M. Tishin, J. A. Rochev, and A. V. Gorelov, Magnetic Carrier and Medical Preparation for Controllable Delivery and Release of Active Substances, Methods of Their Production and Methods of Treatment Using Thereof, US 9,017,713 B2 (2014).
- [21] G. Wehmeyer, T. Yabuki, C. Monachon, J. Wu, and C. Dames, Thermal diodes, regulators, and switches: Physical mechanisms and potential applications, *Appl. Phys. Rev.* **4**, 041304 (2017).
- [22] C. R. Otey, W. T. Lau, and S. Fan, Thermal Rectification through Vacuum, *Phys. Rev. Lett.* **104**, 154301 (2010).
- [23] P. J. van Zwol, K. Joulain, P. Ben Abdallah, J. J. Greffet, and J. Chevrier, Fast nanoscale heat-flux modulation with phase-change materials, *Phys. Rev. B* **83**, 201404 (2011).
- [24] P. J. van Zwol, K. Joulain, P. Ben-Abdallah, and J. Chevrier, Phonon polaritons enhance near-field thermal transfer across the phase transition of  $\text{VO}_2$ , *Phys. Rev. B* **84**, 161413 (2011).
- [25] P. Ben-Abdallah and S.-A. Biehs, Phase-change radiative thermal diode, *Appl. Phys. Lett.* **103**, 191907 (2013).
- [26] P. Ben-Abdallah and S.-A. Biehs, Near-Field Thermal Transistor, *Phys. Rev. Lett.* **112**, 044301 (2014).
- [27] Y. Yang, S. Basu, and L. Wang, Vacuum thermal switch made of phase transition materials considering thin film and substrate effects, *J. Quant. Spectrosc. Radiat. Transfer* **158**, 69 (2015).
- [28] P. J. van Zwol, L. Ranno, and J. Chevrier, Tuning Near Field Radiative Heat Flux through Surface Excitations with a Metal Insulator Transition, *Phys. Rev. Lett.* **108**, 234301 (2012).
- [29] A. Fiorino, D. Thompson, L. Zhu, R. Mittapally, S.-A. Biehs, O. Bezenecet, N. El-Bondry, S. Bansropun, P. Ben-Abdallah, E. Meyhofer, and P. Reddy, A thermal diode based on nanoscale thermal radiation, *ACS Nano* **12**, 5774 (2018).
- [30] L. Remer, E. Mohler, W. Grill, and B. Lüthi, Nonreciprocity in the optical reflection of magnetoplasmas, *Phys. Rev. B* **30**, 3277 (1984).
- [31] W. C. Snyder, Z. Wan, and X. Li, Thermodynamic constraints on reflectance reciprocity and Kirchhoff's law, *Appl. Opt.* **37**, 3464 (1998).
- [32] L. Zhu and S. Fan, Near-complete violation of detailed balance in thermal radiation, *Phys. Rev. B* **90**, 220301 (2014).
- [33] B. Zhao, Y. Shi, J. Wang, Z. Zhao, N. Zhao, and S. Fan, Near-complete violation of Kirchhoff's law of thermal radiation with a 0.3 T magnetic field, *Opt. Lett.* **44**, 4203 (2019).
- [34] Y. Park, V. S. Asadchy, B. Zhao, C. Guo, J. Wang, and S. Fan, Violating Kirchhoff's law of thermal radiation in semitransparent structures, *ACS Photonics* **8**, 2417 (2021).
- [35] K. J. Shayegan, B. Zhao, Y. Kim, S. Fan, and H. A. Atwater, Nonreciprocal infrared absorption via resonant magneto-optical coupling to InAs, *Sci. Adv.* **8**, 1 (2022).
- [36] E. Moncada-Villa, V. Fernández-Hurtado, F. J. García-Vidal, A. García-Martín, and J. C. Cuevas, Magnetic field control of near-field radiative heat transfer and the realization of highly tunable hyperbolic thermal emitters, *Phys. Rev. B* **92**, 125418 (2015).
- [37] E. Moncada-Villa and J. C. Cuevas, Magnetic field effects in the near-field radiative heat transfer between planar structures, *Phys. Rev. B* **101**, 085411 (2020).
- [38] L. Fan, Y. Guo, G. T. Papadakis, B. Zhao, Z. Zhao, S. Budhiraju, M. Orenstein, and S. Fan, Nonreciprocal radiative heat transfer between two planar bodies, *Phys. Rev. B* **101**, 085407 (2020).
- [39] L. Zhu and S. Fan, Persistent Directional Current at Equilibrium in Nonreciprocal Many-Body Near Field

- Electromagnetic Heat Transfer, *Phys. Rev. Lett.* **117**, 134303 (2016).
- [40] P. Ben-Abdallah, Photon Thermal Hall Effect, *Phys. Rev. Lett.* **116**, 084301 (2016).
- [41] D. R. Smith and D. Schurig, Electromagnetic Wave Propagation in Media with Indefinite Permittivity and Permeability Tensors, *Phys. Rev. Lett.* **90**, 077405 (2003).
- [42] R. E. Camley, Nonreciprocal surface waves, *Surf. Sci. Rep.* **7**, 103 (1987).
- [43] Y. Tsurimaki, X. Qian, S. Pajovic, F. Han, M. Li, and G. Chen, Large nonreciprocal absorption and emission of radiation in type-I Weyl semimetals with time reversal symmetry breaking, *Phys. Rev. B* **101**, 165426 (2020).
- [44] Y. Liang, S. Pakniyat, Y. Xiang, J. Chen, F. Shi, G. W. Hanson, and C. Cen, Tunable unidirectional surface plasmon polaritons at the interface between gyrotropic and isotropic conductors, *Optica* **8**, 952 (2021).
- [45] G. Xu, J. Sun, H. Mao, and T. Pan, Near-field radiative thermal modulation enabled by static magnetic fields, *J. Quant. Spectrosc. Radiat. Transfer* **232**, 20 (2019).
- [46] J. Peng, G. Tang, L. Wang, R. Macêdo, H. Chen, and J. Ren, Twist-induced near-field thermal switch using nonreciprocal surface magnon-polaritons, *ACS Photonics* **8**, 2183 (2021).
- [47] Y. Du, J. Peng, Z. Shi, and J. Ren, Twisting the Near-Field Radiative Heat Switch in Hyperbolic Antiferromagnets, (2022).
- [48] Q. Wang, Y. Xu, R. Lou, Z. Liu, M. Li, Y. Huang, D. Shen, H. Weng, S. Wang, and H. Lei, Large intrinsic anomalous Hall effect in half-metallic ferromagnet  $\text{Co}_3\text{Sn}_2\text{S}_2$  with magnetic Weyl fermions, *Nat. Commun.* **9**, 1 (2018).
- [49] P. Li, J. Koo, W. Ning, J. Li, L. Miao, L. Min, Y. Zhu, Y. Wang, N. Alem, C.-X. Liu, Z. Mao, and B. Yan, Giant room temperature anomalous Hall effect and tunable topology in a ferromagnetic topological semimetal  $\text{Co}_2\text{MnAl}$ , *Nat. Commun.* **11**, 3476 (2020).
- [50] A. Markou, D. Kriegner, J. Gayles, L. Zhang, Y.-C. Chen, B. Ernst, Y.-H. Lai, W. Schnelle, Y.-H. Chu, Y. Sun, and C. Felser, Thickness dependence of the anomalous Hall effect in thin films of the topological semimetal  $\text{Co}_2\text{MnGa}$ , *Phys. Rev. B* **100**, 054422 (2019).
- [51] J. Hofmann and S. Das Sarma, Surface plasmon polaritons in topological Weyl semimetals, *Phys. Rev. B* **93**, 241402 (2016).
- [52] Q. Chen, A. R. Kutayiah, I. Oladyshkin, M. Tokman, and A. Belyanin, Optical properties and electromagnetic modes of Weyl semimetals, *Phys. Rev. B* **99**, 075137 (2019).
- [53] B. Zhao, C. Guo, C. A. C. Garcia, P. Narang, and S. Fan, Axion-field-enabled nonreciprocal thermal radiation in Weyl semimetals, *Nano Lett.* **20**, 1923 (2020).
- [54] V. S. Asadchy, C. Guo, B. Zhao, and S. Fan, Subwavelength passive optical isolators using photonic structures based on Weyl semimetals, *Adv. Opt. Mater.* **8**, 2000100 (2020).
- [55] S. Pajovic, Y. Tsurimaki, X. Qian, and G. Chen, Intrinsic nonreciprocal reflection and violation of Kirchhoff's law of radiation in planar type-I magnetic Weyl semimetal surfaces, *Phys. Rev. B* **102**, 165417 (2020).
- [56] G. Xu, J. Sun, and H. Mao, Near-field radiative thermal modulation between Weyl semimetal slabs, *J. Quant. Spectrosc. Radiat. Transfer* **253**, 107173 (2020).
- [57] C. Guo, B. Zhao, D. Huang, and S. Fan, Radiative thermal router based on tunable magnetic Weyl semimetals, *ACS Photonics* **7**, 3257 (2020).
- [58] G. Tang, J. Chen, and L. Zhang, Twist-induced control of near-field heat radiation between magnetic Weyl semimetals, *ACS Photonics* **8**, 443 (2021).
- [59] W. Imamura, L. S. Paixão, É. O. Usuda, N. M. Bom, S. Gama, É. S. N. Lopes, and A. M. G. Carvalho, I-Caloric Effects: A Proposal for Normalization (2018).
- [60] X. Moya and N. D. Mathur, Caloric materials for cooling and heating, *Science* **370**, 797 (2020).
- [61] H. Hou, S. Qian, and I. Takeuchi, Materials, physics and systems for multicaloric cooling, *Nat. Rev. Mater.* **7**, 633 (2022).
- [62] See Supplemental Material at <http://link.aps.org/supplemental/10.1103/PhysRevApplied.20.014053> for the generalization of Figs. 2(a) and 2(b); details on how the magnetocaloric effect  $\Delta T$  is calculated; details on how the reflection coefficients are calculated; a summary of the material property data used in this work; plots of the dielectric tensors of Gd, SiC, and InAs; examples of the spectral heat flux; the transmission coefficient of the Gd-InAs system as a function of  $\theta_B$ ; a survey of some magnetocaloric materials taken from Tishin and Spichkin's textbook [1], consolidated as a plot of  $\theta_C$  against  $\Delta T(B)$  (the data points and original references they used, [63–99], are also included as a table); the transmission coefficient and switching ratios of the Gd-InAs system as a function of the gap width  $d$ ; an overview of how the stray field of the magnetocaloric material can be modeled and its effects on the systems studied in this work.
- [63] T. Hashimoto, T. Numasawa, M. Shino, and T. Okada, Magnetic refrigeration in the temperature range from 10 K to room temperature: The ferromagnetic refrigerants, *Cryogenics (Guildf)* **21**, 647 (1981).
- [64] K. Adachi, Magnetic anisotropy energy in nickel arsenide type crystals, *J. Phys. Soc. Jpn.* **16**, 2187 (1961).
- [65] K. A. Gschneidner, V. K. Pecharsky, and S. K. Malik, in *Advances in Cryogenic Engineering Materials*, edited by L. T. Summers (Springer US, Boston, MA, 1996), pp. 475–483.
- [66] K. A. Gschneidner, V. K. Pecharsky, M. J. Gailloux, and H. Takeya, in *Advances in Cryogenic Engineering Materials*, edited by L. T. Summers (Springer US, Boston, MA, 1996), pp. 465–474.
- [67] P. J. von Ranke, V. K. Pecharsky, and K. A. Gschneidner, Influence of the crystalline electrical field on the magnetocaloric effect of  $\text{DyAl}_2$ ,  $\text{ErAl}_2$ , and  $\text{DyNi}_2$ , *Phys. Rev. B* **58**, 12110 (1998).
- [68] T. Hashimoto, K. Matsumoto, T. Kurihara, T. Numazawa, A. Tomokiyo, H. Yayama, T. Goto, S. Todo, and M. Sahashi, in *Advances in Cryogenic Engineering Materials*, edited by R. P. Reed and A. F. Clark (Springer US, Boston, MA, 1986), pp. 279–286.
- [69] M. Sahashi, H. Niu, Y. Tohkai, K. Inomata, T. Hashimoto, T. Kuzuhara, A. Tomokiyo, and H. Yayama, Specific heat and magnetic entropy associated with magnetic ordering

- in Al-rich  $\text{RAL}_2$  sintered compounds, *IEEE Trans. Magn.* **23**, 2853 (1987).
- [70] W. R. Johanson, G. Pierce, C. B. Zimm, and J. A. Barclay, Heat capacity of  $\text{Gd}_{0.06}\text{Er}_{0.94}\text{Al}_2$  in magnetic fields, *J. Appl. Phys.* **64**, 5892 (1988).
- [71] C. B. Zimm, E. M. Ludeman, M. C. Severson, and T. A. Henning, in *Advances in Cryogenic Engineering*, edited by R. W. Fast (Springer US, Boston, MA, 1992), pp. 883–890.
- [72] B. J. Korte, V. K. Pecharsky, and K. A. Gschneidner, The correlation of the magnetic properties and the magnetocaloric effect in  $(\text{Gd}_{1-x}\text{Er}_x)\text{NiAl}$  alloys, *J. Appl. Phys.* **84**, 5677 (1998).
- [73] L. R. Sill and E. D. Esau, Magnetic characteristics of  $\text{RAGa}$  compounds, *J. Appl. Phys.* **55**, 1844 (1984).
- [74] V. K. Pecharsky, K. A. Gschneidner, and D. Fort, Superheating and other unusual observations regarding the first order phase transition in Dy, *Scr. Mater.* **35**, 843 (1996).
- [75] H. Wada and Y. Tanabe, Giant magnetocaloric effect of  $\text{MnAs}_{1-x}\text{Sb}_x$ , *Appl. Phys. Lett.* **79**, 3302 (2001).
- [76] V. K. Pecharsky, K. A. Gschneidner, S. Y. Dan'kov, and A. M. Tishin, in *Cryocoolers 10*, edited by R. G. Ross (Springer US, Boston, MA, 2002), pp. 639–645.
- [77] F. Canepa, M. Napolitano, and S. Cirafici, Magnetocaloric effect in the intermetallic compound  $\text{Gd}_7\text{Pd}_3$ , *Intermetallics* **10**, 731 (2002).
- [78] V. K. Pecharsky and K. A. Gschneidner, in *Cryocoolers 10*, edited by R. G. Ross (Springer US, Boston, MA, 2002), pp. 629–637.
- [79] K. Selte, A. Kjekshus, A. F. Andresen, and A. Zieba, On the magnetic properties of transition metal substituted  $\text{MnAs}$ , *J. Phys. Chem. Solids* **38**, 719 (1977).
- [80] T. Hashimoto, T. Namasawa, Y. Watanabe, A. Sato, H. Nakagome, O. Horigami, S. Takayama, and M. Watanabe, in *Proceedings of the Ninth International Cryogenic Engineering Conference, 1st ed.* (Butterworth, Guildford, UK, 1982), pp. 26.
- [81] X. Bohigas, J. Tejada, M. Mari'nez-Sarrión, S. Tripp, and R. Black, Magnetic and calorimetric measurements on the magnetocaloric effect in  $\text{La}_{0.6}\text{Ca}_{0.4}\text{MnO}_3$ , *J. Magn. Magn. Mater.* **208**, 85 (2000).
- [82] Y. Sun, M. B. Salamon, and S. H. Chun, Magnetocaloric effect and temperature coefficient of resistance of  $\text{La}_{2/3}(\text{Ca}, \text{Pb})_{1/3}\text{MnO}_3$ , *J. Appl. Phys.* **92**, 3235 (2002).
- [83] Y. Zhang, Z. Liu, H. Zhang, and X. Xu, Direct measurement of thermal behaviour of magnetocaloric effects in perovskite-type  $\text{La}_{0.75}\text{Sr}_x\text{Ca}_{0.25-x}\text{MnO}_3$ , *Mater. Lett.* **45**, 91 (2000).
- [84] T. Bose, R. Chahine, B. Gopal, M. Földeàki, A. Barman, M. Gosh, S. De, and S. Chatterjee, Magnetocaloric properties of the  $\text{La}_{0.7-x}\text{Y}_x\text{Sr}_{0.3}\text{MnO}_3$  giant magnetoresistance ceramics, *Cryogenics (Guildf)* **38**, 849 (1998).
- [85] A. I. Abramovich, A. V. Michurin, O. Y. Gorbenko, and A. R. Kaul, Giant magnetocaloric effect near the Curie temperature in the  $\text{Sm}_{0.6}\text{Sr}_{0.4}\text{MnO}_3$  manganite, *Phys. Solid State* **43**, 715 (2001).
- [86] M. I. Ilyn, A. M. Tishin, K. A. Gschneidner, V. K. Pecharsky, and A. O. Pecharsky, in *Cryocoolers 11*, edited by R. G. Ross (Springer US, Boston, MA, 2002), pp. 457–464.
- [87] P. J. von Ranke, E. P. Nóbrega, I. G. de Oliveira, A. M. Gomes, and R. S. Sarthour, Influence of the crystalline electrical field on the magnetocaloric effect in the series  $\text{RNi}_2$  ( $R = \text{Pr}, \text{Nd}, \text{Gd}, \text{Tb}, \text{Ho}, \text{Er}$ ), *Phys. Rev. B* **63**, 184406 (2001).
- [88] K. A. Gschneidner, H. Takeya, J. O. Moorman, V. K. Pecharsky, S. K. Malik, and C. B. Zimm, in *Advances in Cryogenic Engineering*, edited by P. Kittel (Springer US, Boston, MA, 1994), pp. 1457–1465.
- [89] F. Canepa, M. Napolitano, A. Palenzona, F. Merlo, and S. Cirafici, Magnetocaloric properties of  $\text{GdNiGa}$  and  $\text{GdNiIn}$  intermetallic compounds, *J. Phys. D: Appl. Phys.* **32**, 2721 (1999).
- [90] H. Wada, Y. Tanabe, M. Shiga, H. Sugawara, and H. Sato, Magnetocaloric effects of Laves phase  $\text{Er}(\text{Co}_{1-x}\text{Ni}_x)_2$  compounds, *J. Alloys Compd.* **316**, 245 (2001).
- [91] H. Wada, S. Tomekawa, and M. Shiga, Magnetocaloric properties of a first-order magnetic transition system  $\text{ErCo}_2$ , *Cryogenics (Guildf)* **39**, 915 (1999).
- [92] F. Canepa, P. Manfrinetti, A. Palenzona, S. Cirafici, F. Merlo, and M. Cimberle, Ferromagnetic interactions in  $\text{Nd}_7\text{Co}_6\text{Al}_7$ , *Intermetallics* **8**, 267 (2000).
- [93] X. Y. Liu, J. A. Barclay, R. B. Gopal, M. Földeàki, R. Chahine, T. K. Bose, P. J. Schurer, and J. L. LaCombe, Thermomagnetic properties of amorphous rare-earth alloys with Fe, Ni, or Co, *J. Appl. Phys.* **79**, 1630 (1996).
- [94] M. Földeàki, A. Giguère, B. R. Gopal, R. Chahine, T. K. Bose, X. Y. Liu, and J. A. Barclay, Composition dependence of magnetic properties in amorphous rare-earth-metal-based alloys, *J. Magn. Magn. Mater.* **174**, 295 (1997).
- [95] X. Y. Liu, J. A. Barclay, M. Földeàki, B. R. Gopal, R. Chahine, and T. K. Bose, in *Advances in Cryogenic Engineering Materials*, edited by L. T. Summers (Springer US, Boston, MA, 1996), pp. 431–438.
- [96] X. J. Niu, K. A. Gschneidner, A. O. Pecharsky, and V. K. Pecharsky, Crystallography, magnetic properties and magnetocaloric effect in  $\text{Gd}_4(\text{Bi}_x\text{Sb}_{1-x})_3$  alloys, *J. Magn. Magn. Mater.* **234**, 193 (2001).
- [97] R. Rawat and I. Das, Magnetic transitions in  $\text{CeCu}_{0.86}\text{Ge}_2$  and  $\text{PrCu}_{0.76}\text{Ge}_2$  as studied by magnetocaloric effect, *Phys. Rev. B* **64**, 052407 (2001).
- [98] M. Napolitano, F. Canepa, P. Manfrinetti, and F. Merlo, Magnetic properties and the magnetocaloric effect in the intermetallic compound  $\text{GdFeSi}$ , *J. Mater. Chem.* **10**, 1663 (2000).
- [99] P. B. de Castro, K. Terashima, T. D. Yamamoto, Z. Hou, S. Iwasaki, R. Matsumoto, S. Adachi, Y. Saito, P. Song, H. Takeya, and Y. Takano, Machine-learning-guided discovery of the gigantic magnetocaloric effect in  $\text{HoB}_2$  near the hydrogen liquefaction temperature, *NPG Asia Mater.* **12**, 35 (2020).
- [100] W. Wien, Ueber die Energievertheilung im Emissionsspectrum eines schwarzen Körpers, *Ann. Phys.* **294**, 662 (1896).
- [101] L. Zhang and O. D. Miller, Optimal materials for maximum large-area near-field radiative heat transfer, *ACS Photonics* **7**, 3116 (2020).

- [102] S. A. Maier, *Plasmonics: Fundamentals and Applications*, 1st ed. (Springer Science + Business Media, Inc., New York, 2007).
- [103] A. M. Tishin, Magnetocaloric effect in strong magnetic fields, *Cryogenics (Guildf)*, **30**, 127 (1990).
- [104] N. W. Ashcroft and N. D. Mermin, *Solid State Physics*, 1st ed. (Brooks/Cole, Belmont, CA, 1976).
- [105] O. V. Lounasmaa, Specific Heat of Lutetium Metal Between 0.38 and 4°K, *Phys. Rev.* **133**, A219 (1964).
- [106] S. M. Rytov, *Theory of Electric Fluctuations and Thermal Radiation* (Air Force Cambridge Research Center, Bedford, MA, 1959).
- [107] S.-A. Biehs, P. Ben-Abdallah, F. S. S. Rosa, K. Joulain, and J.-J. Greffet, Nanoscale heat flux between nanoporous materials, *Opt. Express* **19**, A1088 (2011).
- [108] F. Seitz, *The Modern Theory of Solids*, 1st ed. (McGraw-Hill Book Company, Inc, New York, 1940).
- [109] W. G. Spitzer, D. Kleinman, and D. Walsh, Infrared Properties of Hexagonal Silicon Carbide, *Phys. Rev.* **113**, 127 (1959).
- [110] S. Foteinopoulou, G. C. R. Devarapu, G. S. Subramania, S. Krishna, and D. Wasserman, Phonon-polaritonics: Enabling powerful capabilities for infrared photonics, *Nanophotonics* **8**, 2129 (2019).
- [111] K. Seeger, *Semiconductor Physics: An Introduction*, 9th ed. (Springer-Verlag Berlin Heidelberg, New York, 2004).
- [112] O. Madelung, *Semiconductors: Data Handbook*, 3rd ed. (Springer-Verlag Berlin Heidelberg, New York, 2004).
- [113] L. Obied, *Infrared Spectroscopy of Gadolinium* (Brock University, St. Catharines, Canada, 2012).
- [114] J. O. Dimmock and A. J. Freeman, Band Structure and Magnetism of Gadolinium Metal, *Phys. Rev. Lett.* **13**, 750 (1964).
- [115] J. L. Erskine and E. A. Stern, Magneto-optic Kerr effects in gadolinium, *Phys. Rev. B* **8**, 1239 (1973).
- [116] J. Kamarád, J. Kaštil, and Z. Arnold, Practical system for the direct measurement of magneto-caloric effect by micro-thermocouples, *Rev. Sci. Instrum.* **83**, 083902 (2012).
- [117] J. H. Lienhard IV and J. H. Lienhard V, *A Heat Transfer Textbook*, 5th ed. (Phlogiston Press, Cambridge, MA, 2020).
- [118] S. Y. Dan'kov, A. M. Tishin, V. K. Pecharsky, and K. A. Gschneidner, Experimental device for studying the magnetocaloric effect in pulse magnetic fields, *Rev. Sci. Instrum.* **68**, 2432 (1997).
- [119] F. Cugini, G. Porcari, and M. Solzi, Non-contact direct measurement of the magnetocaloric effect in thin samples, *Rev. Sci. Instrum.* **85**, 074902 (2014).
- [120] P. Álvarez-Alonso, J. López-García, G. Daniel-Perez, D. Salazar, P. Lázpita, J. P. Camarillo, H. Flores-Zuñiga, D. Rios-Jara, J. L. Sánchez-Llamazares, and V. A. Chernenko, Simple set-up for adiabatic measurements of magnetocaloric effect, *Key Eng. Mater.* **644**, 215 (2015).
- [121] A. P. Kamantsev, V. V. Koledov, A. V. Mashirov, V. G. Shavrov, N. H. Yen, P. T. Thanh, V. M. Quang, N. H. Dan, A. S. Los, A. Gilewski, I. S. Tereshina, and L. N. Butvina, Measurement of magnetocaloric effect in pulsed magnetic fields with the help of infrared fiber optical temperature sensor, *J. Magn. Magn. Mater.* **440**, 70 (2017).
- [122] F. Cugini and M. Solzi, On the direct measurement of the adiabatic temperature change of magnetocaloric materials, *J. Appl. Phys.* **127**, 123901 (2020).
- [123] M. F. J. Boeije, P. Roy, F. Guillou, H. Yibole, X. F. Miao, L. Caron, D. Banerjee, N. H. van Dijk, R. A. de Groot, and E. Brück, Efficient room-temperature cooling with magnets, *Chem. Mater.* **28**, 4901 (2016).
- [124] A. Narayanaswamy and G. Chen, Surface modes for near field thermophotovoltaics, *Appl. Phys. Lett.* **82**, 3544 (2003).
- [125] S. Boriskina, J. Tong, Y. Huang, J. Zhou, V. Chiloyan, and G. Chen, Enhancement and tunability of near-field radiative heat transfer mediated by surface plasmon polaritons in thin plasmonic films, *Photonics* **2**, 659 (2015).
- [126] O. D. Miller, S. G. Johnson, and A. W. Rodriguez, Effectiveness of Thin Films in Lieu of Hyperbolic Metamaterials in the Near Field, *Phys. Rev. Lett.* **112**, 157402 (2014).
- [127] E. Rousseau, A. Siria, G. Jourdan, S. Volz, F. Comin, J. Chevrier, and J.-J. Greffet, Radiative heat transfer at the nanoscale, *Nat. Photonics* **3**, 514 (2009).
- [128] P. Ben-Abdallah and S.-A. Biehs, Contactless heat flux control with photonic devices, *AIP Adv.* **5**, 053502 (2015).
- [129] Y. Yang and L. Wang, Electrically-controlled near-field radiative thermal modulator made of graphene-coated silicon carbide plates, *J. Quant. Spectrosc. Radiat. Transfer* **197**, 68 (2017).
- [130] Q. Zhao, T. Zhou, T. Wang, W. Liu, J. Liu, T. Yu, Q. Liao, and N. Liu, Active control of near-field radiative heat transfer between graphene-covered metamaterials, *J. Phys. D: Appl. Phys.* **50**, 145101 (2017).
- [131] T. Repän, O. Takayama, and A. Lavrinenko, Hyperbolic surface waves on anisotropic materials without hyperbolic dispersion, *Opt. Express* **28**, 33176 (2020).
- [132] S. Pajovic, Y. Tsurimaki, X. Qian, and S. V. Boriskina, Radiative heat and momentum transfer from materials with broken symmetries: Opinion, *Opt. Mater. Express* **11**, 3125 (2021).
- [133] C. Guo and S. Fan, Theoretical constraints on reciprocal and non-reciprocal many-body radiative heat transfer, *Phys. Rev. B* **102**, 085401 (2020).
- [134] C. Guo and S. Fan, Reciprocity Constraints on Reflection, *Phys. Rev. Lett.* **128**, 256101 (2022).
- [135] C. Guo, B. Zhao, and S. Fan, Adjoint Kirchhoff's Law and General Symmetry Implications for All Thermal Emitters, *Phys. Rev. X* **12**, 21023 (2022).
- [136] J.-P. Mulet, K. Joulain, R. Carminati, and J.-J. Greffet, Enhanced radiative heat transfer at nanometric distances, *Microscale Thermophys. Eng.* **6**, 209 (2002).
- [137] S. Shen, A. Narayanaswamy, and G. Chen, Surface phonon polaritons mediated energy transfer between nanoscale gaps, *Nano Lett.* **9**, 2909 (2009).
- [138] L. Hu, A. Narayanaswamy, X. Chen, and G. Chen, Near-field thermal radiation between two closely spaced glass plates exceeding Planck's Blackbody radiation law, *Appl. Phys. Lett.* **92**, 133106 (2008).
- [139] D. M. Juraschek, P. Narang, and N. A. Spaldin, Phonomagnetic analogs to opto-magnetic effects, *Phys. Rev. Res.* **2**, 043035 (2020).

- [140] D. M. Juraschek, T. Neuman, and P. Narang, Giant effective magnetic fields from optically driven chiral phonons in  $4f$  paramagnets, *Phys. Rev. Res.* **4**, 013129 (2022).
- [141] J. J. Loomis and H. J. Maris, Theory of heat transfer by evanescent electromagnetic waves, *Phys. Rev. B* **50**, 18517 (1994).
- [142] J. B. Pendry, Radiative exchange of heat between nanostructures, *J. Phys. Condens. Matter* **11**, 6621 (1999).
- [143] A. I. Volokitin and B. N. J. Persson, Radiative heat transfer between nanostructures, *Phys. Rev. B* **63**, 205404 (2001).
- [144] P. Wurfel, The chemical potential of radiation, *J. Phys. C Solid State Phys.* **15**, 3967 (1982).
- [145] I. Latella, A. Pérez-Madrid, L. C. Lapas, and J. Miguel Rubi, Near-field thermodynamics: Useful work, efficiency, and energy harvesting, *J. Appl. Phys.* **115**, 124307 (2014).
- [146] W.-C. Hsu, J. K. Tong, B. Liao, Y. Huang, S. V. Boriskina, and G. Chen, Entropic and near-field improvements of thermoradiative cells, *Sci. Rep.* **6**, 34837 (2016).
- [147] H. Iizuka and S. Fan, Exergy in near-field electromagnetic heat transfer, *J. Appl. Phys.* **122**, 124306 (2017).
- [148] L. Zhu, A. Fiorino, D. Thompson, R. Mittapally, E. Meyhofer, and P. Reddy, Near-field photonic cooling through control of the chemical potential of photons, *Nature* **566**, 239 (2019).
- [149] X. Liu and Z. Zhang, Near-field thermal radiation between metasurfaces, *ACS Photonics* **2**, 1320 (2015).
- [150] W. Jin, S. Molesky, Z. Lin, and A. W. Rodriguez, Material scaling and frequency-selective enhancement of near-field radiative heat transfer for lossy metals in two dimensions via inverse design, *Phys. Rev. B* **99**, 41403 (2019).
- [151] Y. Tsurimaki, X. Qian, S. Pajovic, S. Boriskina, and G. Chen, Casimir force among spheres made of Weyl semimetals breaking Lorentz reciprocity, arXiv preprint [arXiv:2109.03809](https://arxiv.org/abs/2109.03809) (2021).
- [152] R. C. O’Handley, *Modern Magnetic Materials: Principles and Applications*, 1st ed. (John Wiley & Sons, Inc, Hoboken, NJ, 2000).
- [153] J. J. Rhyne, in *Magnetic Properties of Rare Earth Metals*, edited by R. J. Elliott (Springer US, Boston, MA, 1972), pp. 129–185.
- [154] M. Krüger, G. Bimonte, T. Emig, and M. Kardar, Trace formulas for nonequilibrium Casimir interactions, heat radiation, and heat transfer for arbitrary objects, *Phys. Rev. B* **86**, 115423 (2012).
- [155] M. T. H. Reid, A. W. Rodriguez, J. White, and S. G. Johnson, Efficient Computation of Casimir Interactions between Arbitrary 3D Objects, *Phys. Rev. Lett.* **103**, 040401 (2009).
- [156] A. W. Rodriguez, M. T. H. Reid, and S. G. Johnson, Fluctuating-surface-current formulation of radiative heat transfer for arbitrary geometries, *Phys. Rev. B* **86**, 220302 (2012).
- [157] A. W. Rodriguez, M. T. H. Reid, and S. G. Johnson, Fluctuating-surface-current formulation of radiative heat transfer: Theory and applications, *Phys. Rev. B* **88**, 054305 (2013).
- [158] M. T. H. Reid and S. G. Johnson, Efficient computation of power, force, and torque in BEM scattering calculations, *IEEE Trans. Antennas Propag.* **63**, 3588 (2015).
- [159] A. G. Polimeridis, M. T. H. Reid, W. Jin, S. G. Johnson, J. K. White, and A. W. Rodriguez, Fluctuating volume-current formulation of electromagnetic fluctuations in inhomogeneous media: Incandescence and luminescence in arbitrary geometries, *Phys. Rev. B* **92**, 134202 (2015).
- [160] B. Sothmann, F. Giazotto, and E. M. Hankiewicz, High-efficiency thermal switch based on topological Josephson junctions, *New J. Phys.* **19**, 23056 (2017).
- [161] F. C. Chen, R. W. Murphy, V. C. Mei, and G. L. Chen, Thermodynamic analysis of four magnetic heat-pump cycles, *J. Eng. Gas Turbines Power* **114**, 715 (1992).
- [162] A. Barman, S. Kar-Narayan, and D. Mukherjee, Caloric effects in perovskite oxides, *Adv. Mater. Interfaces* **6**, 1900291 (2019).